Promoting nitrogen photofixation for the synthesis of ammonia using oxygen-vacant Fe_2O_3/ZrO_2 visible light photocatalyst with straddling heterojunction and enhanced charge transfer.

LAZULI, A.R.S.C., RAMALINGAM, V. and NEPPOLIAN, B.

2024

Supplementary materials are appended after the main text of this document.

Total word count = 5864

Promoting nitrogen photofixation for the synthesis of ammonia using oxygen-vacant Fe_2O_3/ZrO_2 visible light photocatalyst with straddling heterojunction and enhanced charge transfer

*Stesho Crystalin Lazuli A. R.,[a] Vinoth Ramalingam[b] and Neppolian. B[a]**

[a]Energy and Environmental Remediation Lab, Department of Chemistry, SRM Institute of Science and Technology, Kattankulathur, Chennai, Tamil Nadu 603203, India.

[b]School of Engineering, Robert Gordon University, Garthdee Road, Aberdeen AB10 7GJ, United Kingdom.

*Corresponding author: neppolib@srmist.edu.in

Abstract

Photocatalytic nitrogen (N_2) fixation is a promising and environmentally friendly alternative approach to the energy-intensive Haber-Bosch process to produce green ammonia (NH_3) with zero carbon emissions. However, the unique setbacks rest on developing an active photocatalyst with an accelerated charge transfer that could efficiently adsorb and activate the chemically inert N_2 into useful NH_3. Herein, an oxygen-vacant Fe_2O_3/ZrO_2 photocatalyst with straddling heterojunction was successfully synthesised by the hydrothermal method followed by calcination at 450°C. The addition of oxygen vacancy-inducing ferromagnetic material on ZrO_2 increased the adsorption and activation of N_2, broadened the solar absorption window (680 nm extending to 910 nm). It also accelerated light-induced charge separation of the photocatalyst thereby greatly enhancing the production of NH_3 (1.301 mmol h^{-1} g^{-1}) with about a 7-fold increase in comparison to ZrO_2 at ambient conditions under sunlight irradiation. This work therefore sheds light on the effect of oxygen vacancies and the flow of charge carriers in the effective photofixation of N_2 to NH_3 synthesis through a sustainable route.

Keywords: oxygen vacancy; Fe_2O_3/ZrO_2; Type I heterojunction; ferromagnetic; photocatalytic nitrogen reduction

1. Introduction

About 78% of the earth's atmosphere, is an inexhaustible source of free nitrogen (N_2). However, owing to the high bond dissociation energy of N_2 (~ 941 kJ mol^{-1}), it is considered an inert gas as it cannot be easily activated(Bo et al., 2021; Cheng et al., 2019; Han et al., 2020).

The ability to convert the N_2 in the atmosphere to ammonia (NH_3) could lead to a breakthrough in the production of carbon-neutral ammonia. The synthesis of ammonia is prevalent globally due to its demand in various industrial sectors like pharmaceuticals, chemicals, fertilisers, etc. The traditional Haber-Bosch process is an energy-intensive industrial N_2 fixation process employed for decades to produce NH_3(Chen et al., 2021). The anthropogenic carbon dioxide emissions (340 Mt eq/yr) and depletion of fossil fuels (2.5 EJ energy consumption/yr) lead to an urgent global warming mitigation by reducing the environmental impacts of the Haber-Bosch process(Huang et al., 2023a; Liu et al., 2023; Shi et al., 2019; Wei et al., 2022; Zhang et al., 2019. Photocatalytic fixation of solar-driven nitrogen is an ideal pathway to produce ammonia under ambient conditions without using a fossil fuel-based energy system that motivates the transition towards cleaner and more efficient energy utilisation(Ahmad et al., 2023; Babakr et al., 2022; Han et al., 2020; Liu et al., 2022; Tao et al., 2019; Urgesa et al., 2023; Vu et al., 2019; Wang et al., 2022). Since solar energy is a readily available, efficient and renewable source of energy, advanced oxidation processes (AOP) have been employed for the reduction of N_2 photocatalytically. Therefore, the development of efficient photocatalysts that are profoundly light-responsive with adequate charge separation efficiency for the activation of electron-hole pairs is a pressing priority(Abdollahi et al., 2021).

Several unique setbacks in the photofixation of N_2 are mainly due to dinitrogen's huge chemical energy barrier. The photocatalytic conversion of nitrogen to ammonia requires free electrons as it is a 6-electron process. However, photoexcited electron-hole pairs of the photocatalyst recombine quickly due to the short electron lifetime(Amiri et al., 2020). Therefore, a promising photocatalyst for the photofixation of nitrogen should possess good charge carrier mobility, a low recombination rate, and active sites to adsorb nitrogen. Typically, semiconductor photocatalysts with narrow bandgaps enhance the visible-light harnessing efficiency and, therefore, are a research hotspot(Abdollahi et al., 2022; Najafidoust et al., 2022). Additionally, engineering vacancies on the photocatalyst is a prevalent method to design efficient photocatalysts due to their ability to act as active sites. Oxygen vacancies act as an active site to adsorb nitrogen and other photoelectrons on the photocatalyst. The free electrons present in the oxygen-vacant sites are injected into the π^* anti-bonding electrons of dinitrogen, activating it. A new energy-deficient band is generated with an increase in the number of oxygen-vacant sites below the conduction band, producing a new absorption peak that extends to the visible region (400 - 700 nm)(AR et al., 2023; Chen et al., 2021; Kumar et al., 2020; Shen et al., 2022; Shi et al., 2019).

Zirconium oxide (ZrO_2) has recently received significant consideration as a semiconductor photocatalyst due to its high dielectric constant, ion exchange, exceptional chemical, electrical, and optical properties, high thermal stability, and photostable, non-toxic and redox properties(Ananchenko et al., 2022; Boffito et al., 2013; Das et al., 2019; Mou et al., 2019; Neppolian et al., 2011, 2010). Notably, ZrO_2 is a polymorph that can exist as tetragonal (t-ZrO_2), cubic (c-ZrO_2), and monoclinic ZrO_2 (m-ZrO_2) among which, m-ZrO_2 has less symmetrical lattice structure making it a more versatile surface for photocatalytic activity(Keramidas and White, 1974; Matta et al., 1999). Additionally, the surface sites of m-ZrO_2 consist of oxygen vacant sites, surface hydroxyl groups, lewis acid sites, and unsaturated coordinative Zr-O pairs. It is well known that bandgap plays a pivotal role in the selection of a suitable photocatalyst(Singh et al., 2020). The large bandgap of ZrO_2 limited its photocatalytic activity to the ultraviolet region (5% of the solar radiation spectrum). Therefore, the addition of metal oxides or transition metals to ZrO_2 broadens its optical window range to the visible region enhancing its sunlight absorption capability. Doping of pure metals like Er, Ce, Mg, Co, and Fe in ZrO_2 has already been reported to lower the rate of recombination of the light-excited electron-hole charge carriers and reduce their bandgap(Reddy et al., 2019). It is also evident from theoretical calculations that the adsorption energy of nitrogen to ZrO_2 is much lower than that of hydrogen which effectively suppresses the hydrogen evolution reaction thereby promoting the photofixation of nitrogen(Mou et al., 2019; Tao et al., 2019). AR et al. constructed Ni-incorporated ZrO_2/Bi_2O_3 with oxygen-vacant active sites that enhanced the absorption window to the visible spectrum and photoreduction of N_2 with a yield of 9668.2 µmol/h g due to the formation of p-n heterojunction(AR et al., 2023). H Mou et al. fabricated g-C_3N_4/ZrO_2 lamellar composites in their amorphous form by one-step pyrolysis with an optimum ammonium yield of 1446 µmol/h L at 400 nm(Mou et al., 2019). J. Song et al. synthesised a hierarchically structured electrocatalyst made of g-C_3N_4 encapsulated ZrO_2 decorated with CdS QDs (g-C_3N_4@CdS@ZrO_2) that synergistically enhances NRR with an NH_3 yield of 6.32 x 10^{-10} mol/s cm(Song et al., 2021). Recently, R Fu et al. crafted a Ru-loaded ZrO_{2-x} photocatalyst with a Schottky barrier that generated an ammonia rate of 3256 µg/h g at 400 nm(Fu et al., 2023).

Herein, Fe_2O_3 is incorporated with ZrO_2 to efficiently narrow the bandgap of ZrO_2 (~5.0 eV), thereby allowing a flow of electron-hole separation. Fe improves light absorption and photogenerated electron transmission efficiency, enhancing its photocatalytic activity. Ideally, biological nitrogen fixation uses nitrogenase ferroprotein with iron as one of the cofactors for

the conversion of atmospheric N_2 to NH_3. Oftentimes, oxygen-vacant sites are created during the synthesis of the photocatalyst and tend to recombine with the oxygen present in the atmosphere on exposure to air which can be overcome by the introduction of heteroatoms. In this regard, Fe was chosen as the cocatalyst. Oxygen-vacant sites induced by Fe can alter the electron density locally on the adsorbed N_2, thereby lowering the activation energy and enabling the generation of NH_3 through hydrogenation(Curatti et al., 2007; Di et al., 2019; Gao et al., 2017; Hu et al., 2023; Shen et al., 2022; Wang et al., 2014). In the present study, Fe_2O_3/ZrO_2 was synthesized using the hydrothermal method at 170 °C followed by calcination at 450°C. The photocatalyst retained its phase purity and showed superior photofixation of N_2 over bare samples (Fe_2O_3 and ZrO_2) under identical conditions. Furthermore, the influence of ferromaterial (Fe_2O_3) on ZrO_2 improving the charge transfer and oxygen vacancies formed as a result of the heterojunction has been discussed. Orthogonal tests were performed to optimise the nitrogen fixation conditions. This work is designed to efficiently photofix nitrogen at ambient pressure and temperature.

2. Materials and methods

2.1 Materials

Chemicals such as ferric nitrate (SRL, 98%), citric acid monohydrate (SRL, 99.5%), zirconium tetraisopropoxide isopropanol (Sigma Aldrich, 70%), sodium hydroxide (SRL, 97%), nitric acid (SRL, 72%), and isopropyl alcohol (SRL, 99%), sodium potassium tartrate (SRL, 99%), Nessler's reagent (SRL) were purchased and used without further purification. Distilled water with 18.2 MΩ was used for all the synthesis.

2.2 Fabrication of Fe_2O_3/ZrO_2

For the fabrication of Fe_2O_3/ZrO_2, 2M solutions of ferric nitrate and zirconium (IV) isopropoxide were stirred for 20 h in cold conditions separately and then mixed dropwise with vigorous stirring at alkaline conditions (pH = 13). The solution is sonicated for 60 min and then transferred to a Teflon-lined autoclave. (Temperature: 170 °C; Time: 15 h). The obtained product was washed repeatedly and dried at 80 °C overnight. The product calcined at 450°C for 1 h was labelled Fe_2O_3/ZrO_2 (FZ)(AR et al., 2023).

The unary materials were also prepared by the same hydrothermal method using their respective precursors (ferric nitrate solution for Fe_2O_3 and zirconium (IV) isopropoxide solution for ZrO_2).

2.3 Characterisations

X-ray diffraction (XRD, PANalytical) with Cu Kα radiator of λ= 1.5406 A was used to determine the crystal configuration of the photocatalyst. Scanning electron microscope (SEM, Zeus's Sigma 500) and High-resolution transmission electron microscope (HRTEM, FEI Technai G2 F20) were used to detect the surface morphology and structure analysis of the photocatalysts. Fourier-transform infrared spectroscopy (FTIR, IRTracer-100) and X-ray photoelectron spectroscopy (XPS, Physical Electronics) were used to confirm the elemental confirmation and detect the chemical state of the catalyst surface. Electron spin resonance (ESR, Bruner A300 PLUS) was used to measure the vacancies generated by the catalyst. An ultraviolet-visible diffuse reflectance spectrophotometer (UVDRS, SHIMADZU, UV 3600 PLUS) was used to measure the light absorbance and bandgap of the catalyst. The photoluminescence (PL, Agilent fluorescence spectrophotometer) of the catalyst was analysed using a fluorescence chromatograph with an excitation wavelength of 380 nm. A lux meter was used to measure the intensity of the sunlight. For electrochemical measurements, a 3-electrode system was used. Ag/AgCl electrode was used as a reference electrode, a platinum wire was used as the counter electrode and the GC electrode deposited with the catalyst was used as the working electrode.

2.4 Nitrogen photofixation test

The photocatalytic nitrogen fixation tests were performed using a 100 mL Kjeldahl reactor under solar irradiation (65500 lux) at Chennai, India between 10 am and 2 pm. Typically, 50 mL of deionised water was dispersed with 40 mg/L of the as-synthesised photocatalyst and then bubbled with N_2 for half an hour under constant stirring (500 rpm) in the dark. To estimate the amount of ammonia generated, 3 mL of the aliquot was withdrawn initially before light irradiation and then withdrawn every 1 h after irradiation. The concentration of ammonia in the aliquot was analysed using Nessler's method and quantified using a UV spectrometer.

3. Results and discussion

The phase structures and crystallinity of the as-synthesized compounds were analysed using an X-ray diffractometer. The XRD patterns (Fig. 1a) exhibit diffraction peaks of Fe_2O_3, ZrO_2, and Fe_2O_3/ZrO_2 (FZ). For the unary materials, it can be noted that all the diffraction peaks of Fe_2O_3 are indexed to the rhombohedral phase of α-Fe_2O_3 (JCPDS no. 13-0534)(Abbasi et al., 2016) and the diffraction planes of ZrO_2 to the monoclinic phase of ZrO_2 (JCPDS no. 01-

0750)(Yu et al., 2023). The intense peaks at approximately 23.8°, 27.8°, 29.8°, 34.7°, 40.5°, 43.8°, 50.1°, 53.6°, 55.1°, 59.8°, 62.6°, and 65.4° 2 are designated to (110), (-111), (111), (020), (102), (211), (-221), (122), (130), (131), (311), and (-231) planes, respectively, indicating the formation of ZrO_2 in its monoclinic phase (m-ZrO_2). The strong peaks at 24.0°, 33.2°, 35.6°, 40.8°, 49.5°, 54.1°, 57.5°, 62.4°, and 64.1° 2θ (degree) belong to the reflections of (012), (104), (110), (113), (024), (116), (018), (214), and (300), respectively belonging to the pure rhombohedral phase of α-Fe_2O_3. The fabricated binary FZ photocatalyst possesses the diffraction peaks of Fe_2O_3 and ZrO_2, confirming the successful introduction of Fe_2O_3 in ZrO_2. The atoms present in m-ZrO_2 lie on general positions having a C_{2h} space group from which the distribution of normal modes can be calculated.

$$\Gamma = 9\,A_g(R) + 9\,B_g(R) + 8A_u(IR\ E\parallel b) + 7B_u\ (E\perp b) \text{ ---- (1)}$$

The Raman spectrum of the m-ZrO_2 phase has 18 Raman active modes whereas, the t-ZrO_2 and cubic-ZrO_2 phase only have 6 and 1 Raman active modes, respectively. The comparison of the predictions with the observed spectra confirms the formation of the m-ZrO_2 phase, which is the most stable phase of zirconia(Keramidas and White, 1974; Phillippi and Mazdiyasni, 1971). The sharp diffraction peaks of rhombohedral Fe_2O_3 have no other impurities. The Raman spectrum of the obtained Fe_2O_3 (Fig. S 1b) in the range of 200 – 700 cm^{-1} corresponds to the α-Fe_2O_3(Wang et al., 2014). The Raman spectrum of FZ (Fig. S1) also has well-developed bands of both α-Fe_2O_3 and m-ZrO_2. This corroborates the successful fabrication of Fe_2O_3/ZrO_2. On the other hand, the fundamental IR frequencies (Fig. S3) of the synthesized materials between the range of 400-500 cm^{-1} correspond to the M-O chemical bonds. The broad band around the 3500 cm^{-1} region is attributed to the atmospheric moisture retained from the $-OH^-$ groups during synthesis. The minimum bands at 1630 cm^{-1} and 1350 cm^{-1} belong to the most commonly observed absorbed CO_2 and are assigned to the surface carbonate groups in metal oxides(Phillippi and Mazdiyasni, 1971).

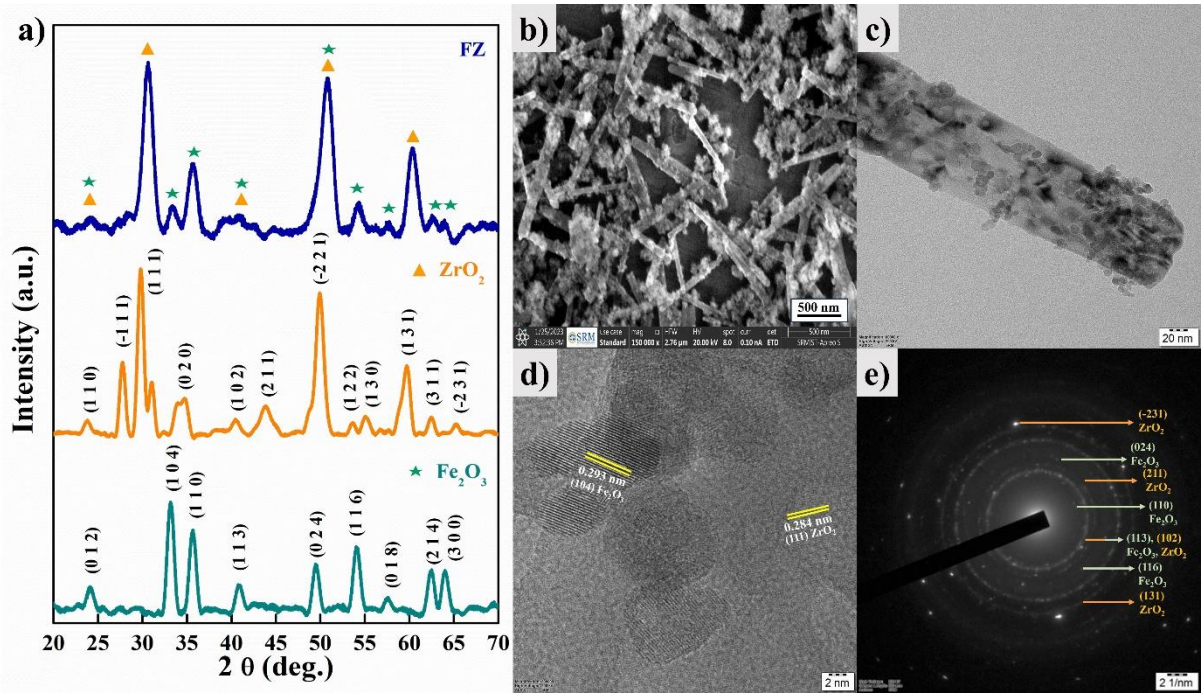

Fig. 1 (a) XRD patterns of Fe_2O_3, ZrO_2, and FZ, (b-e) SEM, TEM, HR-TEM, and SAED images of FZ, respectively.

The structure and morphology of the as-synthesized photocatalysts obtained at 450°C were investigated using SEM and TEM. Fig. 1b-c shows the representative low and high-magnification images of FZ using SEM and TEM, respectively. From Fig. 1 a-b, it is evident that the nanoparticles of Fe_2O_3 (Fig. S4 a) are compactly anchored on the surface of ZrO_2 which maintains its original nanorod structure (Fig. S4 b). The intimate heterojunction thus formed aids in the construction of semiconductor heterostructure interfaces by promoting charge separation to enhance electron-hole separation efficiency. The HR-TEM image obtained for FZ (Fig. 1d) reveals two distinct lattice fringes having interplanar spacings of 0.284 nm and 0.293 nm correlating with the lattice planes of ZrO_2 ($d_{(111)}$) and Fe_2O_3 ($d_{(104)}$), respectively, which match with the planes in the XRD. The Selected Area Electron Diffraction (SAED) pattern of FZ observed in Fig. 1e exhibited a polycrystalline nature. The calculated interplanar distances were found to be representative of (-2 3 1), (2 1 1), (1 0 2), and (1 3 1) planes of ZrO_2 and (0 2 4), (1 1 0), (1 1 3), and (1 1 6) of Fe_2O_3. To further investigate, energy-dispersive X-ray analysis (EDAX) with elemental mapping (Fig. 2, S4 d, S5) was analysed to identify the elemental components and composition (Table S1) of FZ which revealed the uniform distribution of the elements Fe, Zr, and O, confirming the XRD, Raman and XPS results. These experimental results demonstrate the successful establishment of FZ heterojunction between Fe_2O_3 and ZrO_2

206 that is favourable for the rapid transfer of light-generated electrons restraining the
207 recombination of holes and electrons.

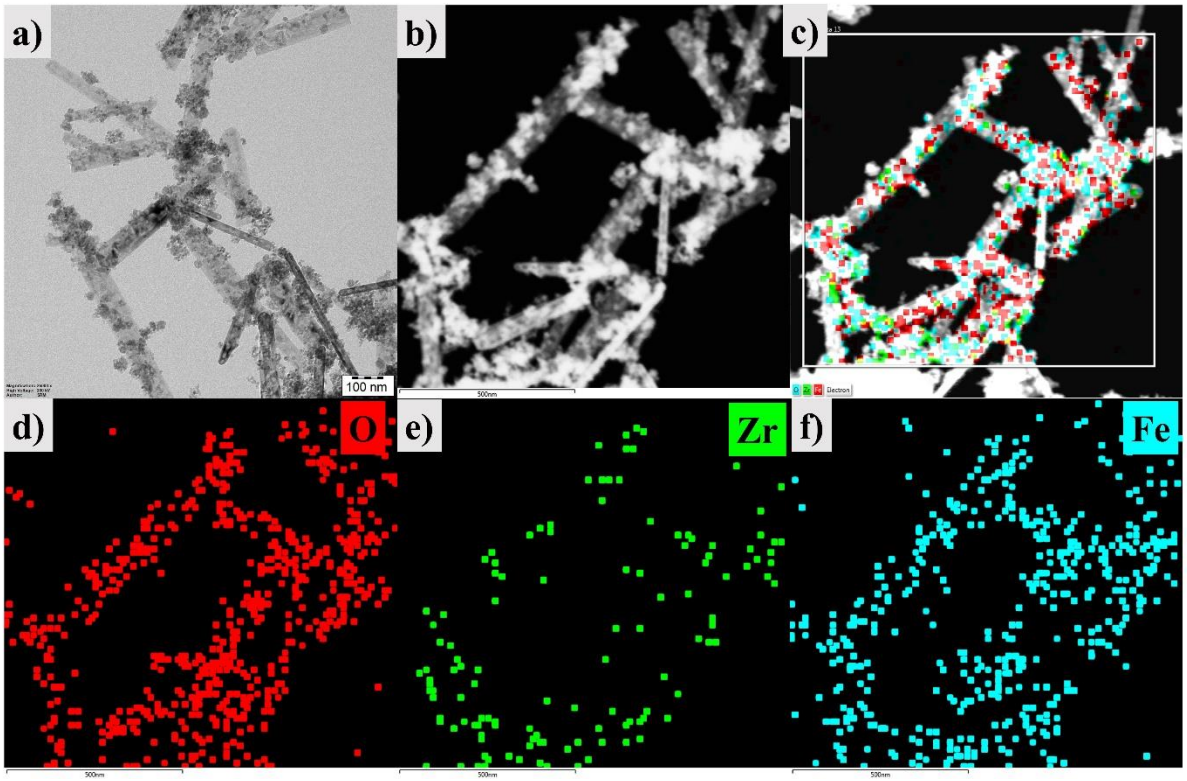

208

209 Fig. 2 a-b) TEM images, and c-f) elemental mapping of FZ.

210

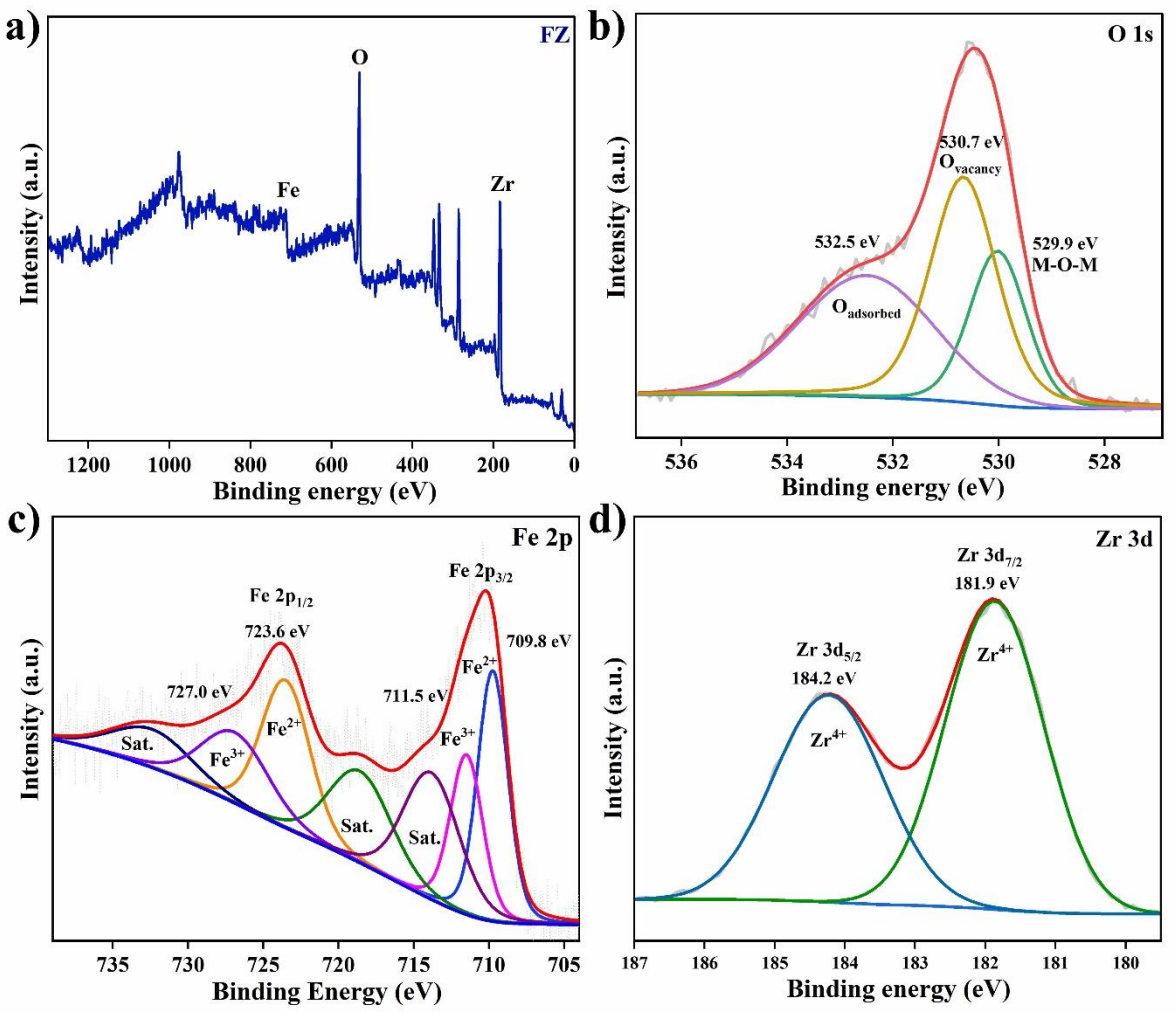

Fig 3. XPS (a) survey spectrum, (b) O 1s, (c) Fe 2p, and (d) Zr 3d of Fe_2O_3/ZrO_2.

To further determine the valence state and elemental composition of the elements present and to gain a deeper insight, XPS analysis was performed on the photocatalysts. Fig. 3a represents the survey spectrum of Fe_2O_3/ZrO_2 composed of the elements O, Fe, and Zr. The deconvoluted XPS spectra (Fig. 3 b-d) of O1s, Fe 2p, and Zr 3d confirm the presence of the elements in their respective oxidation states. Subsequently, the high-resolution XPS spectrum (Fig. 3b) of the O 1s region was resolved into three peaks with binding energies at 529.9 eV, 530.7 eV, and 532.5 eV attributed to the M-O-M, defective oxygen species, and adsorbed oxygen on the surface(AR et al., 2023). To further prove the existence of oxygen vacancies, ESR spectroscopy was performed. Fe_2O_3/ZrO_2 exhibited an ESR signal (Fig. 4d) at a g-value of 2.003, which is attributed to the electrons trapped in the oxygen-vacant sites. The oxygen-vacant sites generate sub-band electrons to get excited speeding up the carrier charge transport and preventing electron-hole pair recombination. The deconvoluted Fe 2p spectra (Fig. 3c) having binding energies at 709.8 eV and 711.5 corresponding to Fe^{2+} and Fe^{3+} of Fe $2p_{3/2}$, and

at 723.6 eV and 727.0 eV corresponding to Fe^{2+} and Fe^{3+} of Fe $2p_{3/2}$, respectively. The integral area at 714.0, 718.9, and 732.8 are attributed to the Fe^{3+} satellite peaks(Xu et al., 2022). Fig. 3 d shows the fitted shapes of Zr 3d spin-orbital splitting peaks with binding energies centered at 181.9 eV and 184.2 eV with a distance of 2.3 eV characteristic for the Zr $3d_{7/2}$ and Zr $3d_{5/2}$ states of Zr^{4+}. The shift in the binding energy of the as-synthesised ZrO_2 (Fig. S9) to commercial ZrO_2 is due to the generation of Zr^{3+} species(AR et al., 2023; Yu et al., 2023).

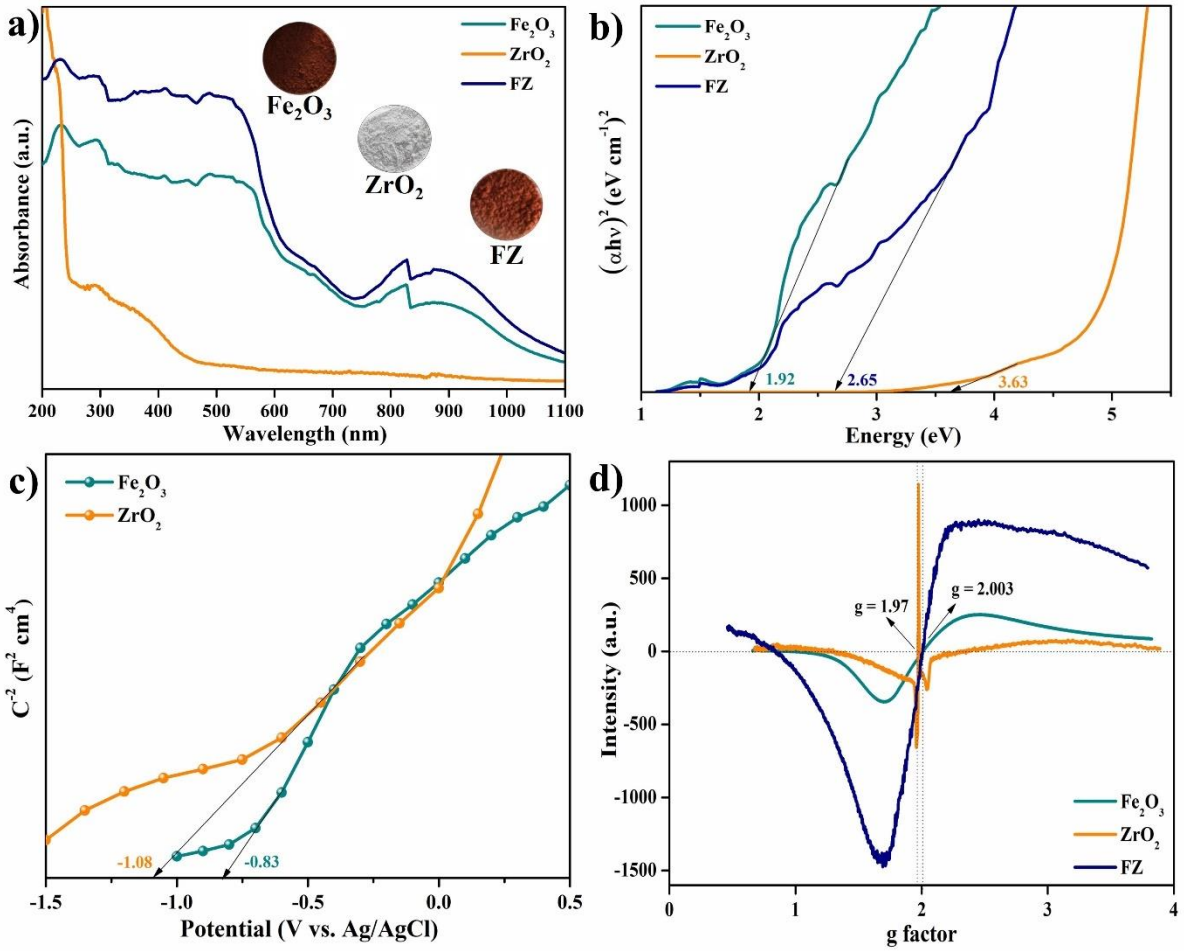

Fig. 4. (a-b) Ultraviolet diffuse reflectance spectra and Tauc plots of Fe_2O_3, ZrO_2, and FZ, respectively, (c) Mott-Schottky curves of Fe_2O_3 and ZrO_2, (d) ESR spectra of Fe_2O_3, ZrO_2, and FZ.

The UVDRS spectra (Fig. 4a) of the photocatalysts were used to identify the absorption edges and band gaps using Kubelka-Munk formulae. The energy band gap (Fig. 4b) of the catalysts was carried out using Tauc relations plotted with (α hυ) vs. energy, where, α is the Kubelka-Munk coefficient and the incident photon energy is represented as hυ. FZ has a visible-light active photocatalyst absorption edge of 680 nm extending to 910 nm with a bandgap (E_g) of 2.65 eV. In comparison, Fe_2O_3 and ZrO_2 have an absorption edge of 653 nm

to 887 nm and 255 nm to 498 nm, with bandgaps estimated to be 1.92 eV and 3.63 eV, respectively. The incorporation of iron with ZrO_2 enhanced the light-harvesting property of the photocatalyst FZ from the UV-visible region to the visible region. The Mott-Schottky plots (Fig. 4c) of Fe_2O_3 and ZrO_2 indicate that the semiconductors are n-type having positive slopes. The -0.83 V and -1.08 V vs Ag/AgCl flat band potentials were obtained from the Mott-Schottky plots for Fe_2O_3 and ZrO_2, respectively. Consequently, the conduction band (CB) edge potentials for Fe_2O_3 and ZrO_2 are -0.93 V and -1.18 V vs Ag/AgCl, respectively. When illuminated under sunlight, Fe_2O_3 and ZrO_2 generate photon-induced electrons and holes at the CB and VB edges of the photocatalysts. The band gap of the semiconductor Fe_2O_3 is completely contained in the band gap of ZrO_2 (Fig. 7) and, therefore, undergoes Type-I heterojunction with a straddling band structure. Consequently, the holes and electrons are accumulated at the VB and CB edges of Fe_2O_3. Generally, oxygen vacancies can be identified from the absorption bands in UVDRS but remain questionable. In this respect, the oxygen vacancies, being paramagnetic, are successfully studied and determined at the atomistic level by electron spin resonance (ESR) in most oxides. The oxygen-vacant sites identified from the ESR spectra naturally serve as effective electron traps. The ESR spectra (Fig. 4d, Fig. S11) show a signal centred at g = 1.97 attributed to Zr^{3+} ions and another minor signal was observed at g = 2.003 assigned to single electrons trapped in oxygen-vacant sites of ZrO_2. The paramagnetic center (Zr^{3+}) is a result of the reduction of Zr^{4+} ions due to the capture of electrons from the neighbouring oxygen-vacant site(Matta et al., 1999; Slipenyuk et al., 2004). The ESR signals of Fe_2O_3 and FZ centred at g = 2.003 correspond to the spin-unpaired electrons introduced by oxygen-vacant sites confirming the existence of oxygen vacancies(Al-Madanat et al., 2021; Ananchenko et al., 2022). The magnetic hysteresis (M-H) curves (Fig. S12) indicated the Fe_2O_3 and ZrO_2 behaviour to be ferromagnetic and diamagnetic, respectively. The FZ on forming the heterojunction still possesses ferromagnetic properties in small amounts. Since there is a built-in internal electric field due to their spontaneous ferroelectric polarisation in ferroelectric materials, there is the spatial separation of the charges resulting in the flow of the light-excited charge carriers in the opposite direction which in turn reduces the recombination rate and increases the efficiency of the photocatalyst(Gao et al., 2017).

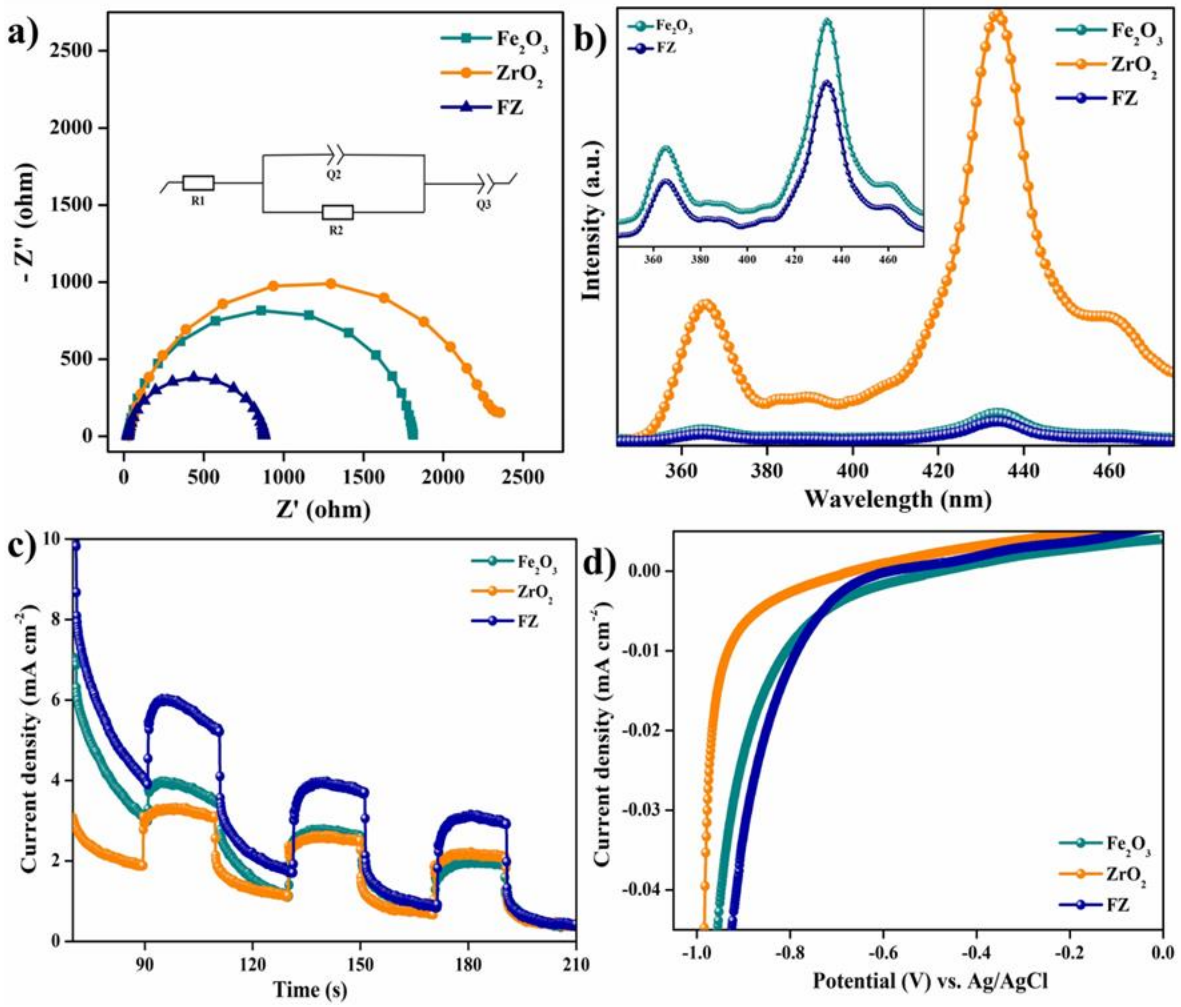

Fig. 5. (a-d) EIS spectra, Photoluminescence, Transient photocurrent responses, and Linear Sweep Voltammetry of Fe_2O_3, ZrO_2, and FZ, respectively.

The separation efficiencies of the light-induced charge carriers were determined using electrochemical impedance spectra (EIS), photoluminescence (PL) emission spectra and transient photocurrent responses. The EIS and transient photocurrent curves were employed to measure the interfacial charge transfer kinetics of the as-synthesised materials. EIS measures the charge carrier resistance of the photocatalysts by correlating the resistance of the charge carrier with the radius of the semicircle. Typically, when the Nyquist curve radius is smaller, the charge transfer resistance is lower, facilitating efficient charger carrier separation, and resulting in more efficient and faster electron transfer. Positively, the Nyquist curve in Fig. 5a exhibited a smaller radius, with a lower charge transfer resistance for FZ than Fe_2O_3 and ZrO_2. The photons stimulate the electrons in the semiconductor which are trapped by holes when illuminated, increasing the photocurrent initially. The photocatalysts on subjection to photons at a 20 s cyclic period presented a quick and steady anodic photocurrent response (Fig. 5c). FZ

exhibited a stable and higher photocurrent than Fe_2O_3 and ZrO_2. Typically, a decrease in PL peak intensity is observed when there is a decrease in recombination of electron-hole pair and vice versa. Steady-state PL spectroscopy was used to investigate the recombination of the photogenerated electron-hole pairs. The large photoluminescence intensity of ZrO_2 has obstructed its photocatalytic effect due to its rapid recombination rate of the photon-excited charge carriers. FZ exhibited a lower-intensity PL emission peak, indicating a suppressed recombination and a greater charge carrier separation than Fe_2O_3 and ZrO_2 (Fig. 5b). The efficient separation of charges is due to the influence of the heterojunction formed on the photocatalyst FZ. The linear sweep voltammogram (LSV) curves (Fig. 5d) of the photocatalysts obtained show an early onset potential for the FZ photocatalyst in comparison to the unary materials due to its improved transfer of charge carriers. which is consistent with the impedance, photocurrent responses, and PL measurements.

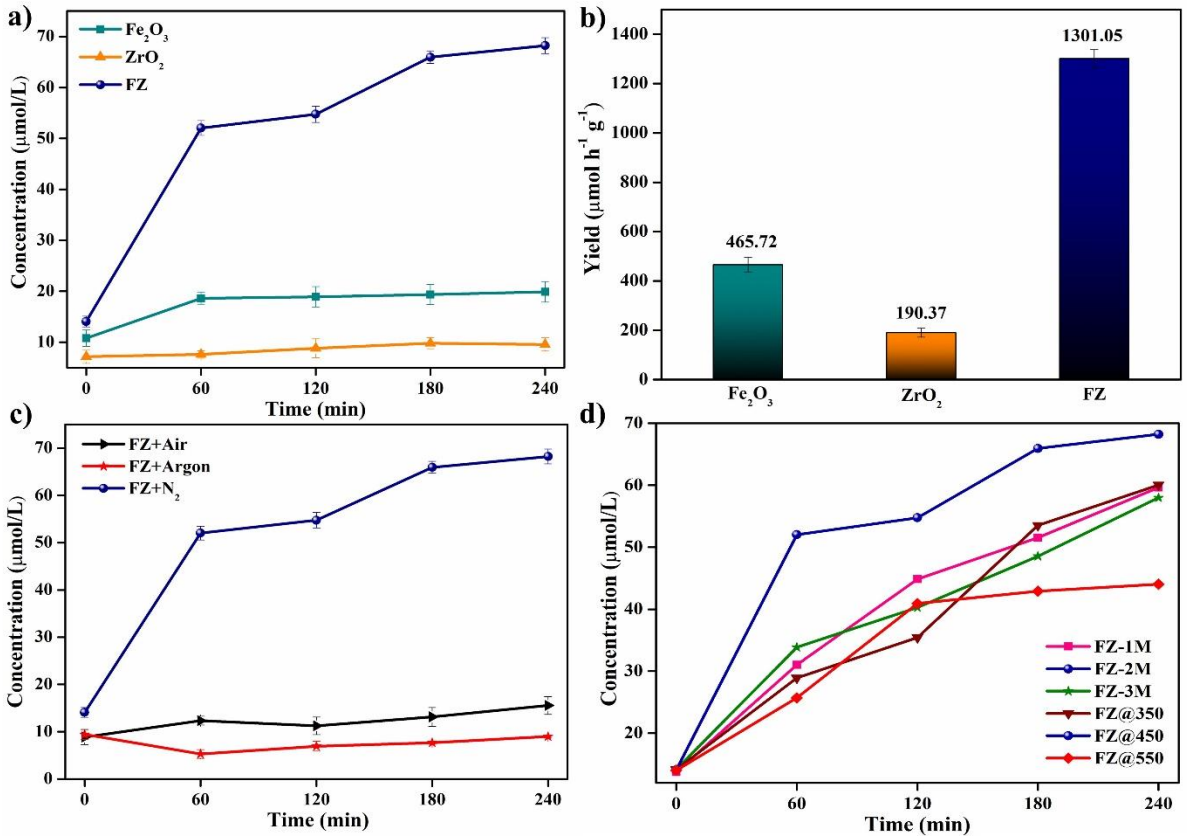

Fig. 6. (a-b) Quantitative determination of ammonia generated using the as-synthesised photocatalysts, (c) control experiments with FZ in air, Ar, and N_2, and (d) optimisation studies.

The photocatalytic reduction experiments on Fe_2O_3, ZrO_2, and FZ under sunlight irradiation were performed under various reaction conditions as observed in Fig. 6. Fe_2O_3 and ZrO_2 generated ammonia of about 465.72 µmol h^{-1} g^{-1} and 190.37 µmol h^{-1} g^{-1}, respectively.

Conventionally, a Type I or straddling heterojunction has the formation of a close interface between two unequal band-structured semiconductors that are in contact with each other in such a way that the generated photoelectrons and holes migrate from the semiconductor with a more negative conductive band and positive valence band to the other semiconductor. FZ exhibited Type I heterojunction (Fig. 7) wherein, the excitons of ZrO_2 migrated to Fe_2O_3. The electrons on Fe_2O_3 were then trapped in a sub-level formed by the oxygen-vacant sites suppressing the direct recombination of the generated excitons. Some of the photoexcited electrons trapped by the oxygen-vacant sites in Fe_2O_3 further aid in the reduction of N_2 to NH_3 enhancing its photocatalytic activity. The presence of heterojunction and oxygen vacancies not only inhibits the recombination of excitons directly but also effectively reduces N_2 by utilising the trapped electron(Lee et al., 2021; Rajamani et al., 2024; Yin et al., 2019). The FZ with straddling heterojunction has an enhanced ammonia production rate of 1301.05 μmol h^{-1} g^{-1} in comparison to the unary photocatalysts. The formation of heterojunction in FZ proved to improve the photoreduction of nitrogen under sunlight at atmospheric conditions owing to the efficient separation of charges between the unary materials. The addition of Fe_2O_3 increases the number of oxygen-vacant sites and plays a pivotal role in the adsorption and activation of dinitrogen. Orthogonal tests were performed under various reaction conditions to optimise and confirm ammonia production (Fig. S13). Control experiments without nitrogen, light or the photocatalyst confirmed the necessity for N_2, sunlight, and the photocatalyst as important requisites for the photocatalytic reduction of nitrogen to ammonia under ambient conditions (Fig. S14). Furthermore, a steady increase in ammonia generation with time proves that the ammonia produced is not from the probable impurities present in the reaction system.

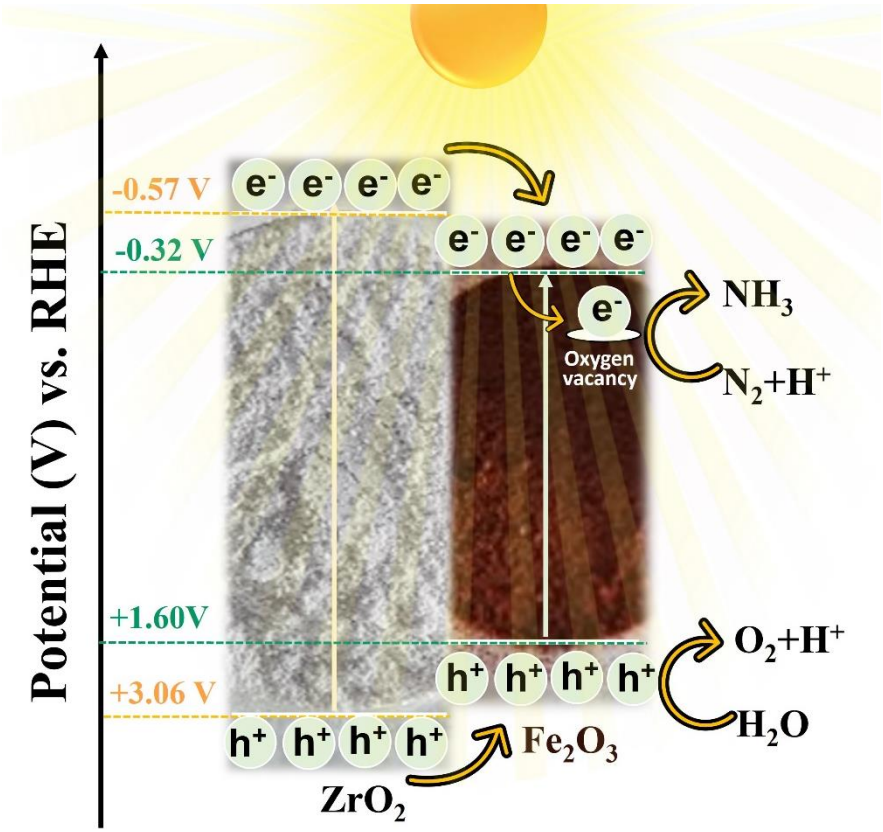

Fig. 7. Plausible mechanism

4. Conclusions

In summary, Fe_2O_3/ZrO_2 obtained through hydrothermal treatment followed by calcination is an n-type semiconductor photocatalyst with Type I heterojunction that allows the separation of charges favourably. The obtained FZ heterojunction photocatalyst generates about 7-fold ammonia (1301.05 µmol h^{-1} g^{-1}) in comparison to ZrO_2 (190.37 µmol h^{-1} g^{-1}) due to its accelerated transfer of photo-excited charge carriers and low recombination rate. The employment of ZrO_2 with an oxygen vacancy-inducing ferromagnetic material not only enables the adsorption and activation of nitrogen but also reduces the recombination rate of the photocatalyst thereby enhancing the production of ammonia at ambient conditions under solar irradiation. This work provides promising results guiding the development of novel photocatalysts that could further enhance the photofixation of nitrogen. The future of photocatalytic nitrogen fixation holds promise for sustainable nitrogen utilization. Further research is needed to develop efficient photocatalyst materials and integrated systems, enhancing nitrogen fixation under visible light irradiation. Advancements in reactor design and engineering are crucial for scaling up photocatalytic processes for practical applications in fertilizer production and environmental remediation.

Acknowledgements

This article was financially supported by Department of Science and Technology-Water Technology Initiative (DST-WTI) [Ref no.: DST/TMD/EWO/WTI/2K19/EWFH/2019/169] and Department of Science and Technology-Promotion of University Research and Scientific Excellence (DST-PURSE) [File no.: SR/PURSE/2021/65].

References

Abbasi, A., Ghanbari, D., Salavati-Niasari, M., Hamadanian, M., 2016. Photo-degradation of methylene blue: photocatalyst and magnetic investigation of Fe 2 O 3–TiO 2 nanoparticles and nanocomposites. Journal of materials science: Materials in electronics 27, 4800–4809.

Abdollahi, B., Farshnama, S., Asl, E.A., Najafidoust, A., Sarani, M., 2022. Cu (BDC) metal–organic framework (MOF)-based Ag2CrO4 heterostructure with enhanced solar-light degradation of organic dyes. Inorg Chem Commun 138, 109236.

Abdollahi, B., Najafidoust, A., Asl, E.A., Sillanpaa, M., 2021. Fabrication of ZiF-8 metal organic framework (MOFs)-based CuO-ZnO photocatalyst with enhanced solar-light-driven property for degradation of organic dyes. Arabian Journal of Chemistry 14, 103444.

Ahmad, H.A., Ahmed, S.S., Amiri, O., 2023. Simple synthesis of CeFeO3 nanostructures as an efficient visible-light-driven photocatalyst in degradation of Congo red dye: Mechanism investigation. Int J Hydrogen Energy 48, 3878–3892.

Al-Madanat, O., Nunes, B.N., AlSalka, Y., Hakki, A., Curti, M., Patrocinio, A.O.T., Bahnemann, D.W., 2021. Application of EPR spectroscopy in TiO2 and Nb2O5 photocatalysis. Catalysts 11, 1514.

Amiri, O., Salar, K., Othman, P., Rasul, T., Faiq, D., Saadat, M., 2020. Purification of wastewater by the piezo-catalyst effect of PbTiO3 nanostructures under ultrasonic vibration. J Hazard Mater 394, 122514.

Ananchenko, D. V, Nikiforov, S. V, Sobyanin, K. V, Konev, S.F., Dauletbekova, A.K., Akhmetova-Abdik, G., Akilbekov, A.T., Popov, A.I., 2022. Paramagnetic Defects and Thermoluminescence in Irradiated Nanostructured Monoclinic Zirconium Dioxide. Materials 15, 8624.

AR, S.C.L., Thapa, R., Neppolian, B., 2023. Photon driven nitrogen fixation via Ni-incorporated ZrO2/Bi2O3: pn heterojunction. Catal Today 420, 114034.

Babakr, K.A., Amiri, O., Guo, L.J., Rashi, M.A., Mahmood, P.H., 2022. Kinetic and thermodynamic study in piezo degradation of methylene blue by SbSI/Sb2S3 nanocomposites stimulated by zirconium oxide balls. Sci Rep 12, 15242.

Bo, Y., Wang, H., Lin, Y., Yang, T., Ye, R., Li, Y., Hu, C., Du, P., Hu, Y., Liu, Z., 2021. Altering hydrogenation pathways in photocatalytic nitrogen fixation by tuning local

electronic structure of oxygen vacancy with dopant. Angewandte Chemie International Edition 60, 16085–16092.

Boffito, D.C., Crocellà, V., Pirola, C., Neppolian, B., Cerrato, G., Ashokkumar, M., Bianchi, C.L., 2013. Ultrasonic enhancement of the acidity, surface area and free fatty acids esterification catalytic activity of sulphated ZrO2–TiO2 systems. J Catal 297, 17–26.

Chen, S., Liu, D., Peng, T., 2021. Fundamentals and Recent Progress of Photocatalytic Nitrogen-Fixation Reaction over Semiconductors. Solar Rrl 5, 2000487.

Cheng, M., Xiao, C., Xie, Y., 2019. Photocatalytic nitrogen fixation: the role of defects in photocatalysts. J Mater Chem A Mater 7, 19616–19633.

Curatti, L., Hernandez, J.A., Igarashi, R.Y., Soboh, B., Zhao, D., Rubio, L.M., 2007. In vitro synthesis of the iron–molybdenum cofactor of nitrogenase from iron, sulfur, molybdenum, and homocitrate using purified proteins. Proceedings of the National Academy of Sciences 104, 17626–17631.

Das, R.S., Warkhade, S.K., Kumar, A., Wankhade, A. V, 2019. Graphene oxide-based zirconium oxide nanocomposite for enhanced visible light-driven photocatalytic activity. Research on Chemical Intermediates 45, 1689–1705.

Di, L., Yang, H., Xian, T., Liu, X., Chen, X., 2019. Photocatalytic and photo-Fenton catalytic degradation activities of Z-scheme Ag2S/BiFeO3 heterojunction composites under visible-light irradiation. Nanomaterials 9, 399.

Fu, R., Wang, Y., Wang, G., Zhan, Q., Zhang, L., Liu, L., 2023. Defective ZrO 2− x supported Ru nanoparticles as a Mott–Schottky photocatalyst for efficient ammonia synthesis under ambient conditions. Green Chemistry 25, 8531–8538.

Gao, B., Yang, C., Chen, J., Ma, Y., Xie, J., Zhang, H., Wei, L., Li, Q., Du, J., Xu, Q., 2017. Ferromagnetic photocatalysts of FeTiO 3–Fe 2 O 3 nanocomposites. RSC Adv 7, 54594–54602.

Han, H., Yang, Y., Liu, J., Zheng, X., Wang, X., Meng, S., Zhang, S., Fu, X., Chen, S., 2020. Effect of Zn vacancies in Zn3In2S6 nanosheets on boosting photocatalytic N2 fixation. ACS Appl Energy Mater 3, 11275–11284.

Hu, T., Jiang, G., Yan, Y., Lan, S., Xie, J., Zhang, Q., Li, Y., 2023. Facile synthesis of Fe single-atom porous photocatalysts via direct metal atomization achieving efficient photocatalytic nitrogen fixation. J Mater Sci Technol 167, 248–257.

Huang, X., Shi, Y., Liu, C., Wang, Z., Bi, J., Jimmy, C.Y., Wu, L., 2023. Enhanced photocatalytic nitrogen fixation on Cu2O clusters/MIL-100 (Fe) heterojunction. Appl Surf Sci 640, 158443.

Keramidas, V.G., White, W.B., 1974. Raman scattering study of the crystallization and phase transformations of ZrO2. Journal of the American Ceramic Society 57, 22–24.

Kumar, T.R.N., Karthik, P., Neppolian, B., 2020. Polaron and bipolaron induced charge carrier transportation for enhanced photocatalytic H 2 production. Nanoscale 12, 14213–14221.

Lee, J., Tan, L.-L., Chai, S.-P., 2021. Heterojunction photocatalysts for artificial nitrogen fixation: fundamentals, latest advances and future perspectives. Nanoscale 13, 7011–7033.

Liu, X., Han, X., Liang, Z., Xue, Y., Zhou, Y., Zhang, X., Cui, H., Tian, J., 2022. Phosphorous-doped 1T-MoS2 decorated nitrogen-doped g-C3N4 nanosheets for enhanced photocatalytic nitrogen fixation. J Colloid Interface Sci 605, 320–329.

Liu, Y.-H., Huang, P.-W., Hatzell, M.C., 2023. A rotating ring disc electrode study of photo (electro) catalyst for nitrogen fixation. Faraday Discuss.

Matta, J., Lamonier, J.-F., Abi-Aad, E., Zhilinskaya, E.A., Aboukaïs, A., 1999. Transformation of tetragonal zirconia phase to monoclinic phase in the presence of Fe 3+ ions as probes: an EPR study. Physical Chemistry Chemical Physics 1, 4975–4980.

Mou, H., Wang, J., Yu, D., Zhang, D., Chen, W., Wang, Y., Wang, D., Mu, T., 2019. Fabricating amorphous g-C3N4/ZrO2 photocatalysts by one-step pyrolysis for solar-driven ambient ammonia synthesis. ACS Appl Mater Interfaces 11, 44360–44365.

Najafidoust, A., Abdollahi, B., Asl, E.A., Karimi, R., 2022. Synthesis and characterization of novel M@ ZnO/UiO-66 (M= Ni, Pt, Pd and mixed Pt&Pd) as an efficient photocatalyst under solar light. J Mol Struct 1256, 132580.

Neppolian, B., Ciceri, L., Bianchi, C.L., Grieser, F., Ashokkumar, M., 2011. Sonophotocatalytic degradation of 4-chlorophenol using Bi2O3/TiZrO4 as a visible light responsive photocatalyst. Ultrason Sonochem 18, 135–139.

Neppolian, B., Kim, Y., Ashokkumar, M., Yamashita, H., Choi, H., 2010. Preparation and properties of visible light responsive ZrTiO4/Bi2O3 photocatalysts for 4-chlorophenol decomposition. J Hazard Mater 182, 557–562.

Phillippi, C.M., Mazdiyasni, K.S., 1971. Infrared and Raman spectra of zirconia polymorphs. Journal of the American Ceramic Society 54, 254–258.

Rajamani, M., Jeyaprakash, J.S., Madhavan, J., Neppolian, B., 2024. Turning trash to treasure: Innovative use of exhausted desiccant waste supported zinc indium sulphide for sustainable photocatalytic abatement of tetracycline. Chemosphere 349, 140969.

Reddy, C.V., Reddy, I.N., Akkinepally, B., Harish, V.V.N., Reddy, K.R., Jaesool, S., 2019. Mn-doped ZrO2 nanoparticles prepared by a template-free method for electrochemical energy storage and abatement of dye degradation. Ceram Int 45, 15298–15306.

Shen, Y., Shou, J., Chen, L., Han, W., Zhang, L., Chen, Y., Tu, X., Zhang, S., Sun, Q., Chang, Y., 2022. Efficient photocatalytic nitrogen fixation from air under sunlight via iron-doped WO3. Appl Catal A Gen 643, 118739.

Shi, R., Zhao, Y., Waterhouse, G.I.N., Zhang, S., Zhang, T., 2019. Defect engineering in photocatalytic nitrogen fixation. ACS Catal 9, 9739–9750.

Singh, H., Yadav, K.K., Bajpai, V.K., Jha, M., 2020. Tuning the bandgap of m-ZrO2 by incorporation of copper nanoparticles into visible region for the treatment of organic pollutants. Mater Res Bull 123, 110698.

Slipenyuk, A.M., Glinchuk, M.D., Bykov, I.P., Ragulya, A. V, Klimenko, V.P., Konstantinova, T.E., Danilenko, I.A., 2004. ESR investigation of yttria stabilized zirconia powders with nanosize particles. Ferroelectrics 298, 289–296.

Song, J., Dai, J., Zhang, P., Liu, Y., Yu, J., Ding, B., 2021. gC 3 N 4 encapsulated ZrO 2 nanofibrous membrane decorated with CdS quantum dots: A hierarchically structured, self-supported electrocatalyst toward synergistic NH 3 synthesis. Nano Res 14, 1479–1487.

Tao, H., Choi, C., Ding, L.-X., Jiang, Z., Han, Z., Jia, M., Fan, Q., Gao, Y., Wang, H., Robertson, A.W., 2019. Nitrogen fixation by Ru single-atom electrocatalytic reduction. Chem 5, 204–214.

Urgesa, M.H., Wolde, G.S., Kuo, D.-H., 2023. One-step hydrothermal synthesis of novel flower-like Bi2Mn4O10 anchored on BiOI1− xBrx nanosheets for efficient photocatalytic nitrogen fixation. J Alloys Compd 947, 169589.

Vu, M., Sakar, M., Hassanzadeh-Tabrizi, S.A., Do, T., 2019. Nitrogen Fixation: Photo (electro) catalytic Nitrogen Fixation: Problems and Possibilities (Adv. Mater. Interfaces 12/2019). Adv Mater Interfaces 6, 1970076.

Wang, L., Lu, X., Han, C., Lu, R., Yang, S., Song, X., 2014. Electrospun hollow cage-like α-Fe 2 O 3 microspheres: synthesis, formation mechanism, and morphology-preserved conversion to Fe nanostructures. CrystEngComm 16, 10618–10623.

Wang, X., Wang, B., Yin, S., Xu, M., Yang, L., Sun, H., 2022. Highly efficient photocatalytic nitrogen fixation on bio-inspired triphase interface with improved diffusion of nitrogen. J Clean Prod 360, 132162.

Wei, Y., Jiang, W., Liu, Y., Bai, X., Hao, D., Ni, B.-J., 2022. Recent advances in photocatalytic nitrogen fixation and beyond. Nanoscale.

Xu, Y., Zhang, H., Gong, D., Chen, Y., Xu, S., Qiu, P., 2022. Solar water splitting with nanostructured hematite: the role of oxygen vacancy. J Mater Sci 57, 19716–19729.

Yin, J., Xing, Z., Kuang, J., Li, Z., Zhu, Q., Zhou, W., 2019. Dual oxygen vacancy defects-mediated efficient electron-hole separation via surface engineering of Ag/Bi2MoO6 nanosheets/TiO2 nanobelts ternary heterostructures. Journal of Industrial and Engineering Chemistry 78, 155–163.

Yu, X., Zhou, C., Huang, Z., Xin, C., Lin, Y., Fu, F., Li, S., Zhang, W., 2023. Rational design of AgCl@ Zr3+-ZrO2 nanostructures for ultra-efficient visible-light photodegradation of emerging pollutants. Appl Catal B 325, 122308.

Zhang, S., Zhao, Y., Shi, R., Waterhouse, G.I.N., Zhang, T., 2019. Photocatalytic ammonia synthesis: Recent progress and future. EnergyChem 1, 100013.

Highlights

- Green ammonia production using renewable energy sources (water and sunlight)
- Fe_2O_3/ZrO_2 heterojunction is fabricated via ultrasound-assisted hydrothermal method
- Amplification of charge separation using ferromagnetic material
- Enhanced adsorption and activation of the non-polar, inert N_2 molecule using oxygen-vacancies
- Superior ammonia production (1.301 mmol h^{-1} g^{-1}) without the use of sacrificial agents

Graphical abstract

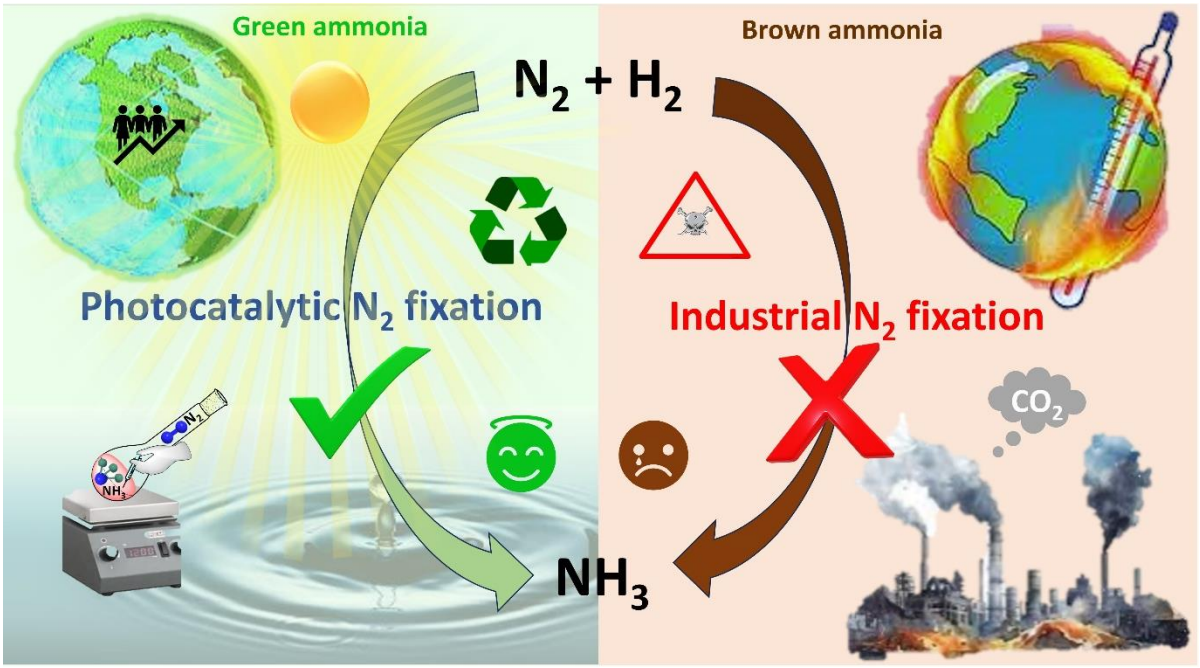

Promoting nitrogen photofixation for the synthesis of ammonia using oxygen-vacant Fe_2O_3/ZrO_2 visible light photocatalyst with straddling heterojunction and enhanced charge transfer

*A. R. Stesho Crystalin Lazuli[a], Vinoth Ramalingam[b], Bernaurdshaw Neppolian[a]**

[a]Energy and Environmental Remediation Lab, Department of Chemistry, SRM Institute of Science and Technology, Kattankulathur, Chennai, Tamil Nadu 603203, India.

[b]School of Engineering, Robert Gordon University, Garthdee Road, Aberdeen AB10 7GJ, United Kingdom.

*Corresponding author: neppolib@srmist.edu.in

Methods

Synthesis of FZ in various concentrations

For the fabrication of Fe_2O_3/ZrO_2, 2M solutions of ferric nitrate and zirconium (IV) isopropoxide were stirred for 20 h in cold conditions separately and then mixed dropwise with vigorous stirring at alkaline conditions (pH = 13). The solution was sonicated for 60 min and then transferred to a 100 mL autoclave. (Temperature: 170 °C; Time: 15 h). The obtained product was washed repeatedly and dried at 80 °C overnight. The product calcined at 450°C for 1 h was labelled Fe_2O_3/ZrO_2 (FZ-2M)) as it is in the molar ratio of 2:2.

To optimise the ratio of Fe_2O_3 and ZrO_2, different molar ratios (1M and 3M) of Fe_2O_3 were prepared using the same hydrothermal method followed by the same calcination temperature and labelled as FZ-1M and FZ-3M, respectively.

Synthesis of FZ at different calcination temperatures

For the fabrication of Fe_2O_3/ZrO_2, 2M solutions of ferric nitrate and zirconium (IV) isopropoxide were stirred for 20 h in cold conditions separately and then mixed dropwise with vigorous stirring at alkaline conditions (pH = 13). The solution was sonicated for 60 min and then transferred to a 100 mL autoclave. (Temperature: 170 °C; Time: 15 h). The obtained product was washed repeatedly and dried at 80 °C overnight. The product calcined at 450°C for 1 h was labelled Fe_2O_3/ZrO_2 (FZ@450).

To optimise the calcination temperature of FZ, Fe_2O_3/ZrO_2 prepared using the same hydrothermal method was calcined at different temperatures (350°C and 550°C) and labelled as FZ@350 and FZ@550, respectively.

Results and discussion

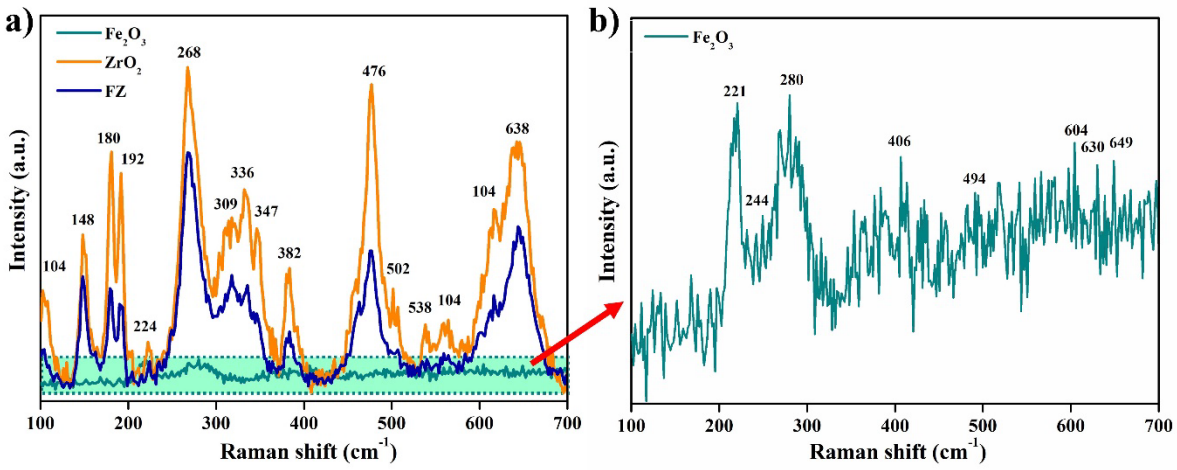

Fig. S1 a) Raman spectra of Fe_2O_3, ZrO_2, and FZ, b) enlarged Raman spectra of Fe_2O_3.

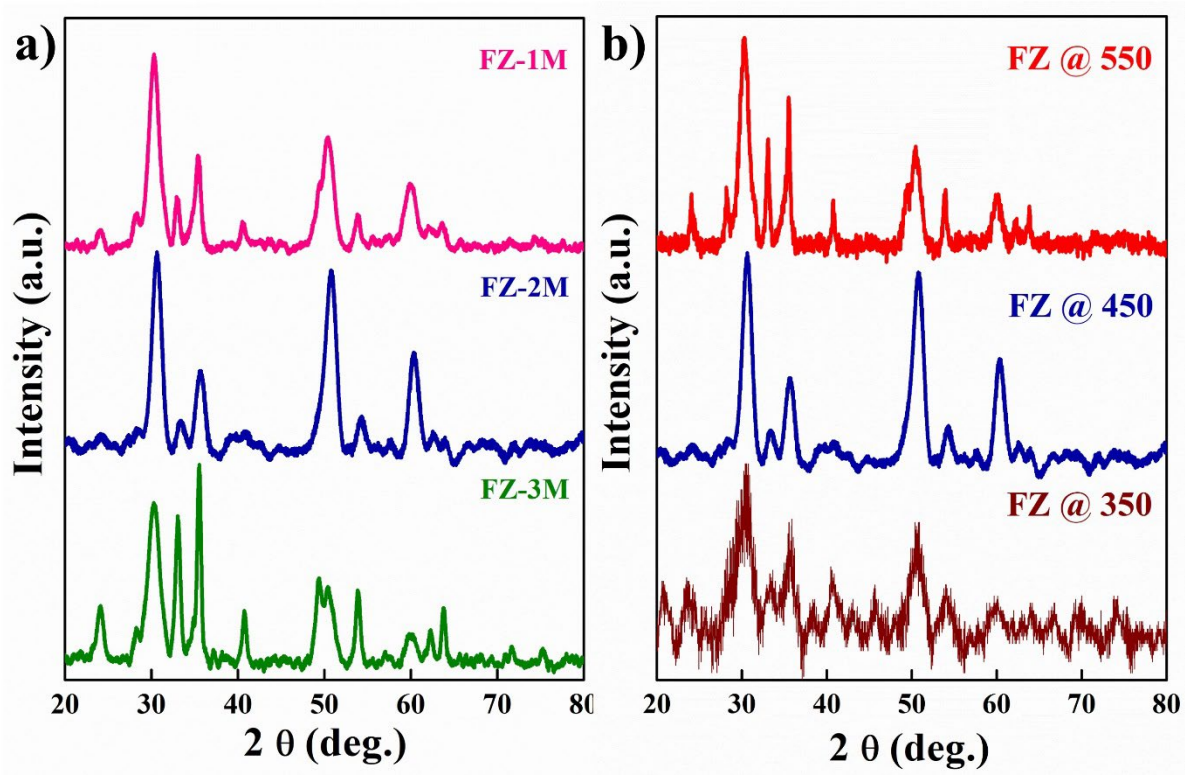

Fig. S2 (a,b) XRD spectra of FZ in various molar concentrations and FZ calcined at different temperatures, respectively.

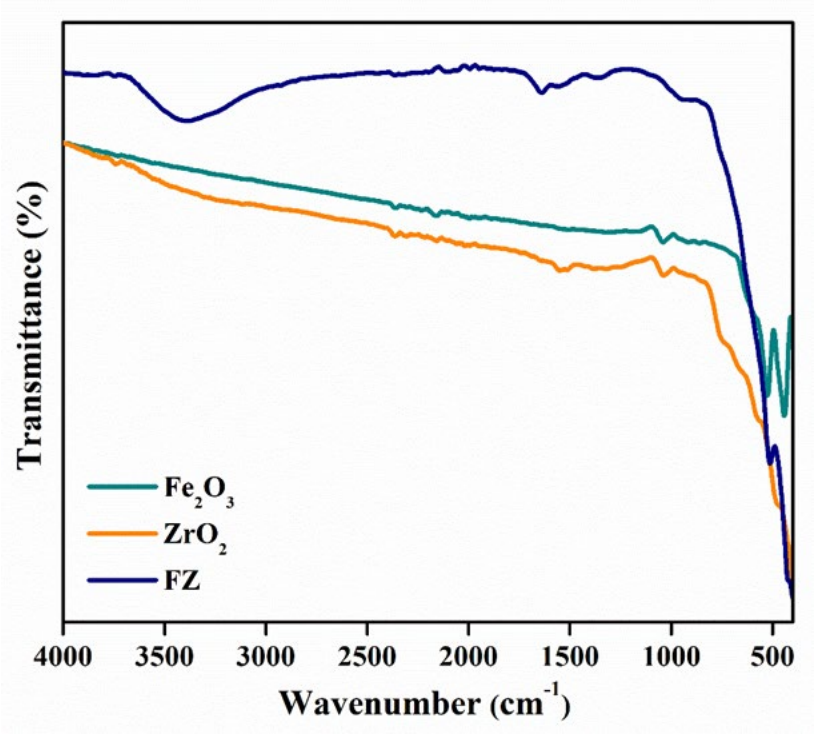

Fig. S3 FTIR spectra of Fe_2O_3, ZrO_2, and FZ.

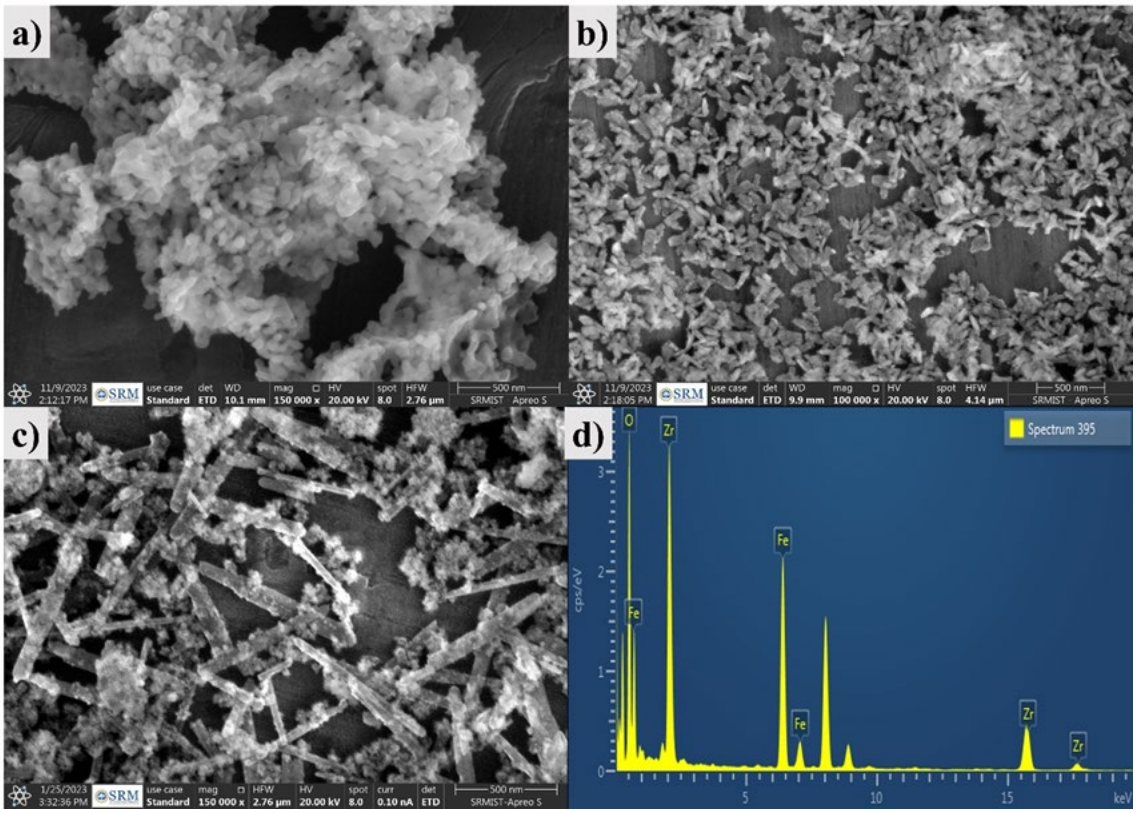

Fig. S4 a-c) SEM images of Fe_2O_3, ZrO_2, and FZ, respectively and d) EDAX spectrum of FZ.

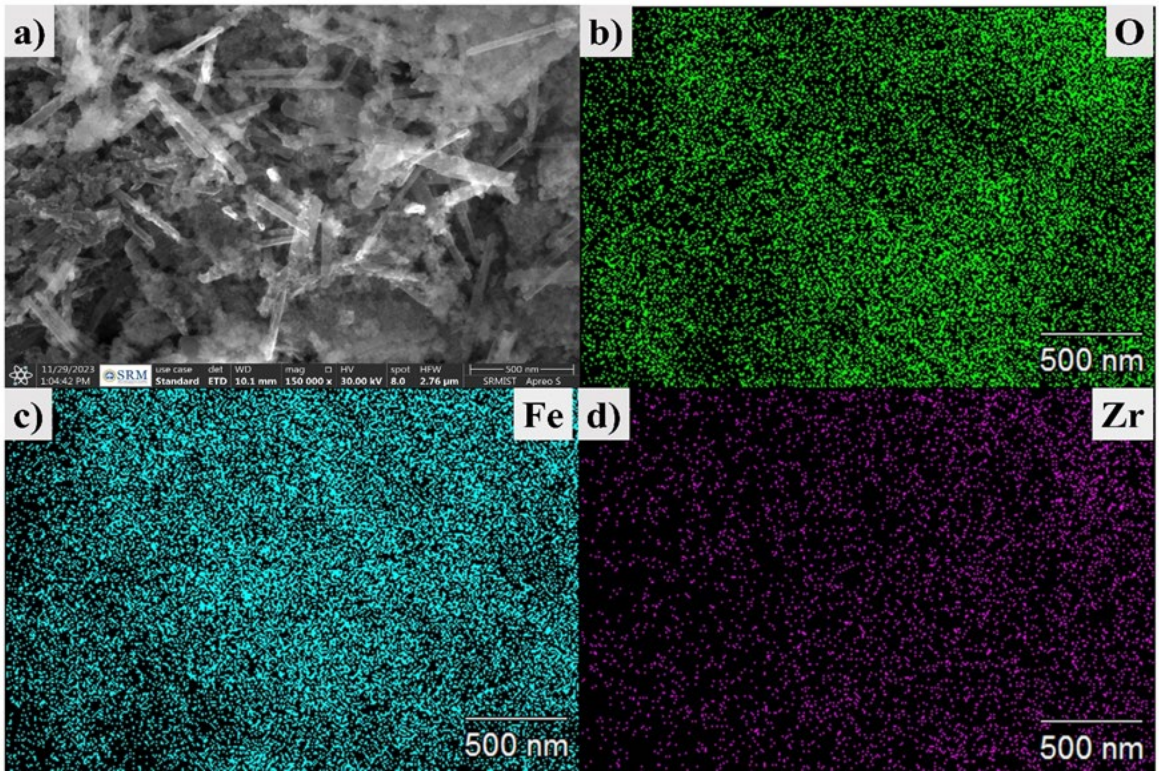

Fig. S5 a-f) SEM image and elemental mapping of FZ.

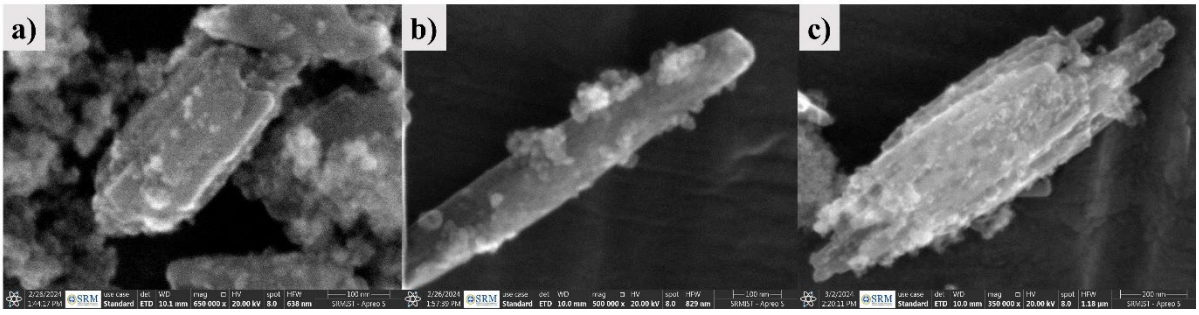

Fig. S6 SEM images of FZ synthesised in various molar ratios: a) FZ-1M, FZ-2M, and FZ-3M, respectively.

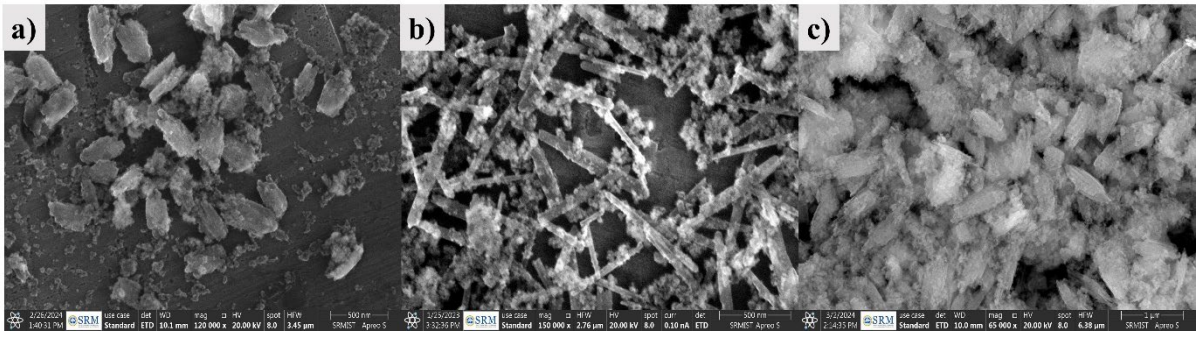

Fig. S7 a-c) SEM images of FZ@350, FZ@450, and FZ@550, respectively.

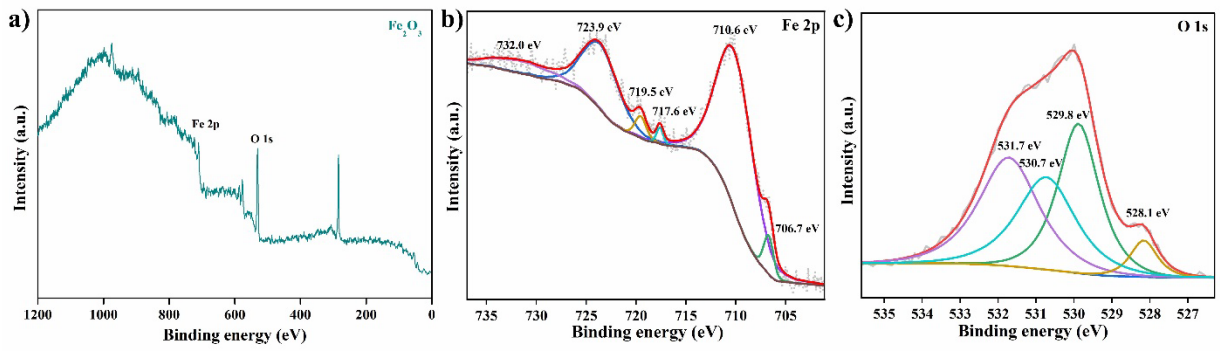

Fig. S8 XPS spectra of a) Survey scan b) Fe 2p and c) O 1s of Fe_2O_3.

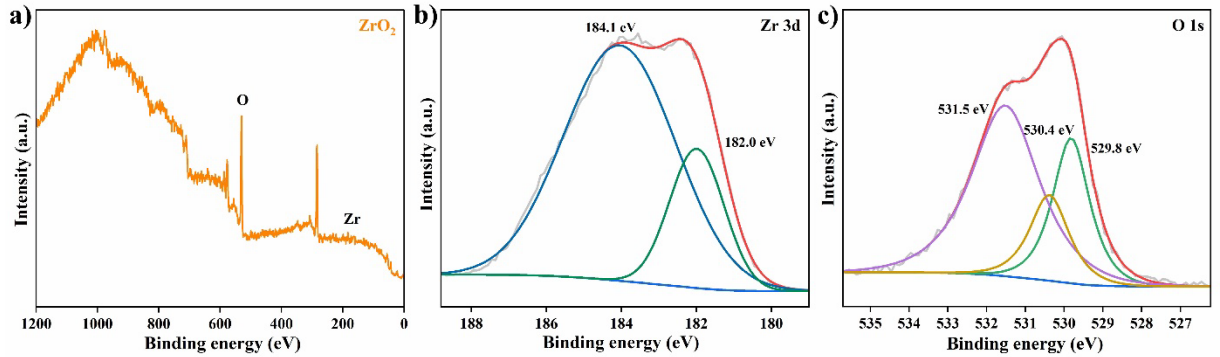

Fig. S9 XPS spectra of a) Survey scan b) Zr 3d and c) O 1s of ZrO_2.

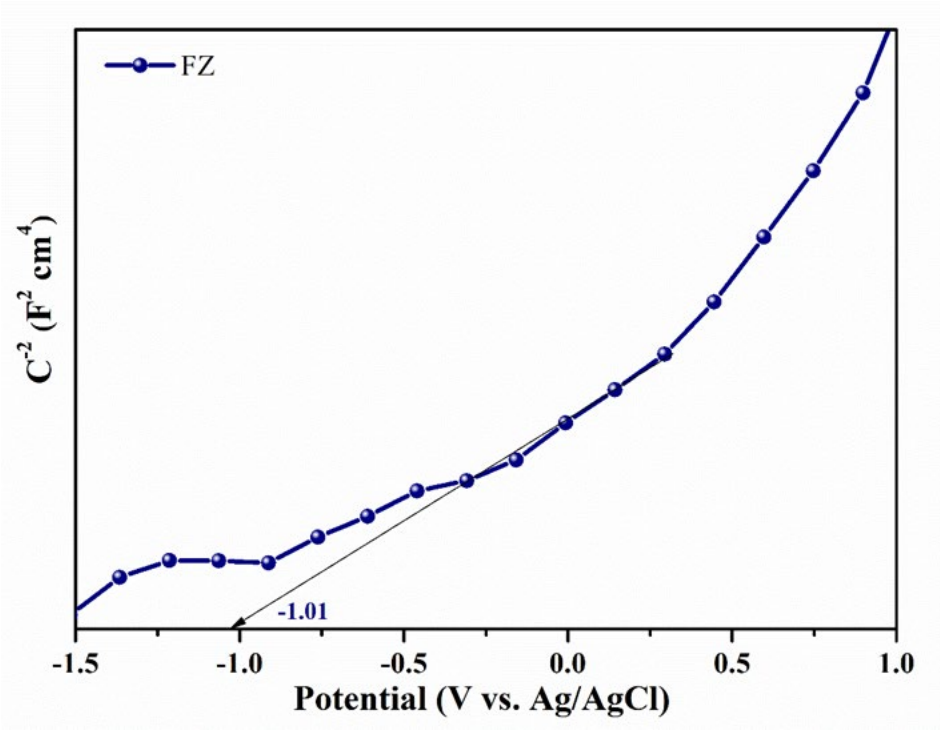

Fig. S10 Mott-Schottky plot of FZ.

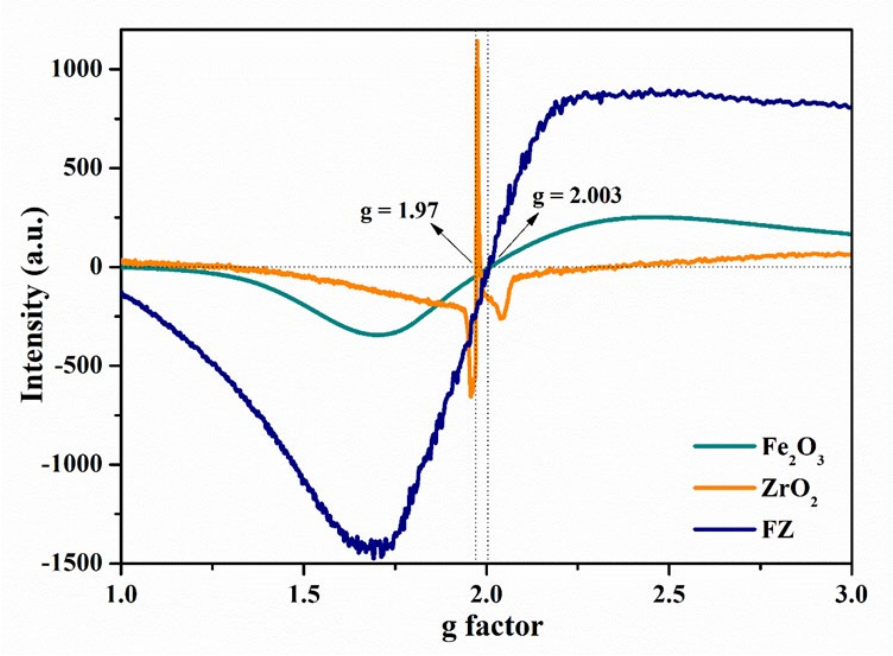

Fig. S11 Enhanced ESR spectra of Fe_2O_3, ZrO_2, and FZ.

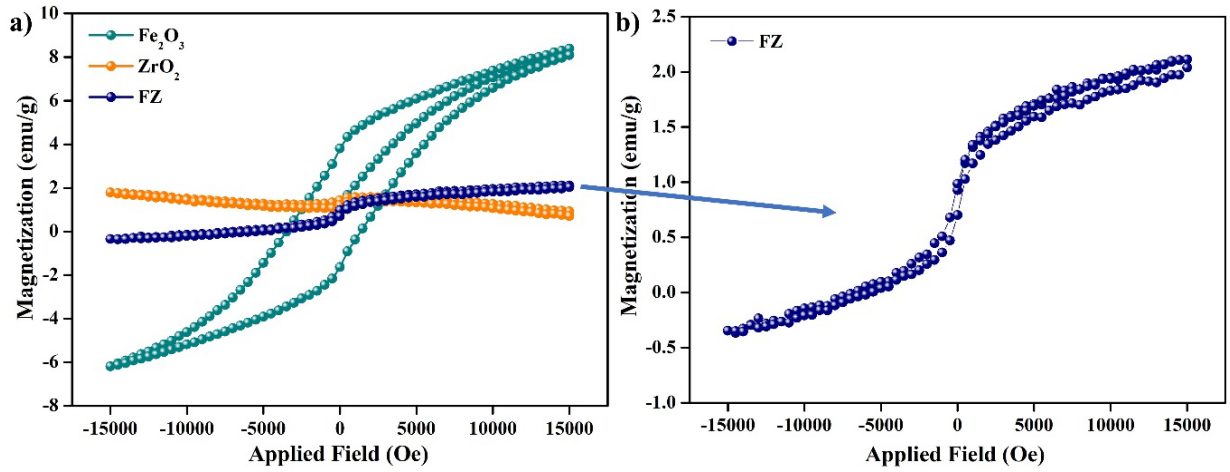

Fig. S12 a) Magnetic hysteresis (M-H) Fe_2O_3, ZrO_2, and FZ curves, b) enlarged magnetic hysteresis (M-H) FZ curves.

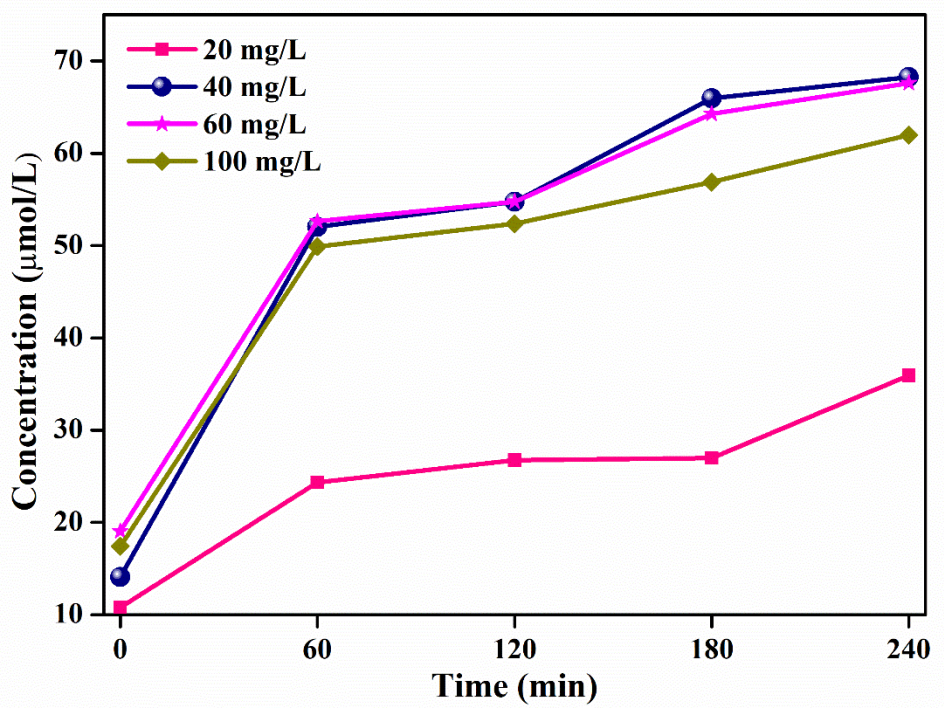

Fig. S13 The effect of photocatalyst dosage on the photocatalytic fixation of N_2.

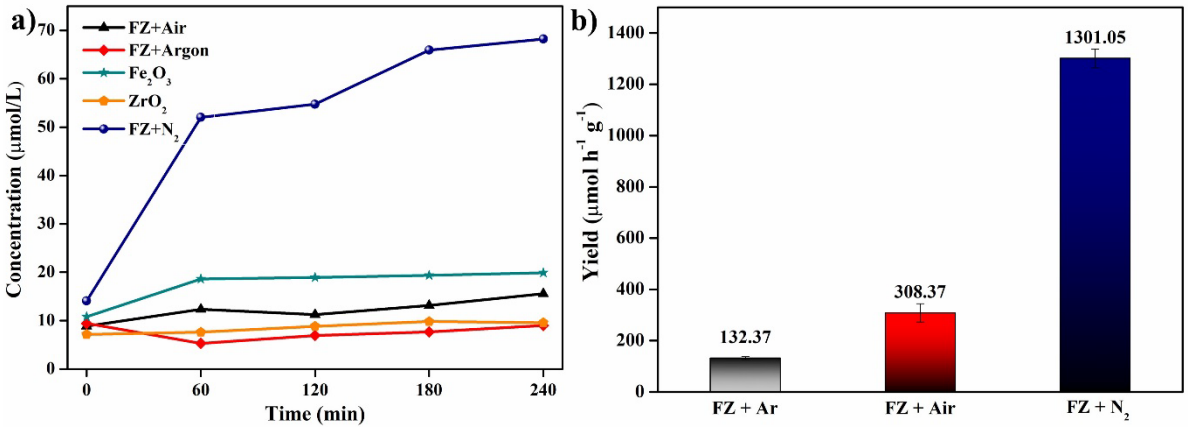

Fig. S14 Comparison of the photocatalytic activity of the photocatalyst with control experiments.

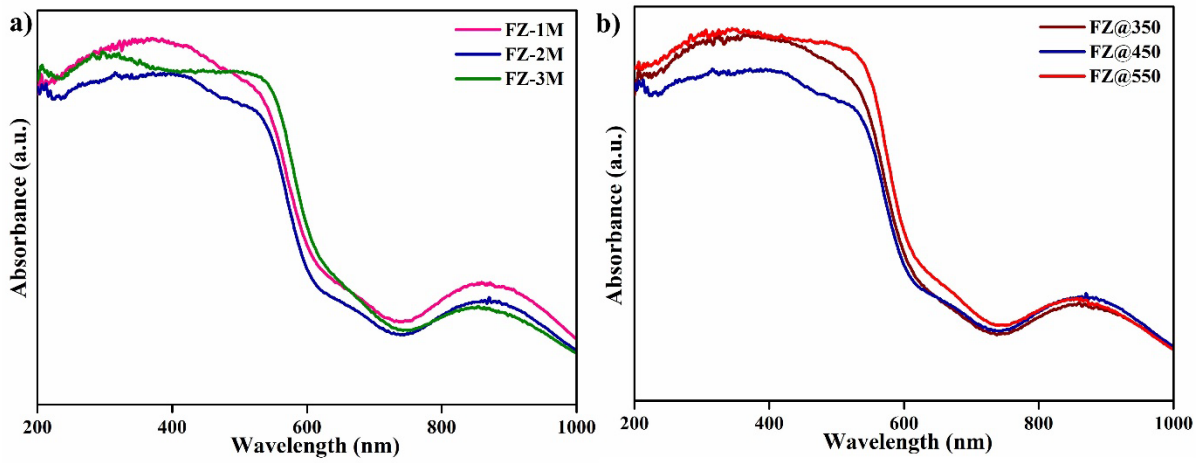

Fig. S15 (a,b) UVDRS spectra of FZ in various molar concentrations and FZ calcined at different temperatures, respectively.

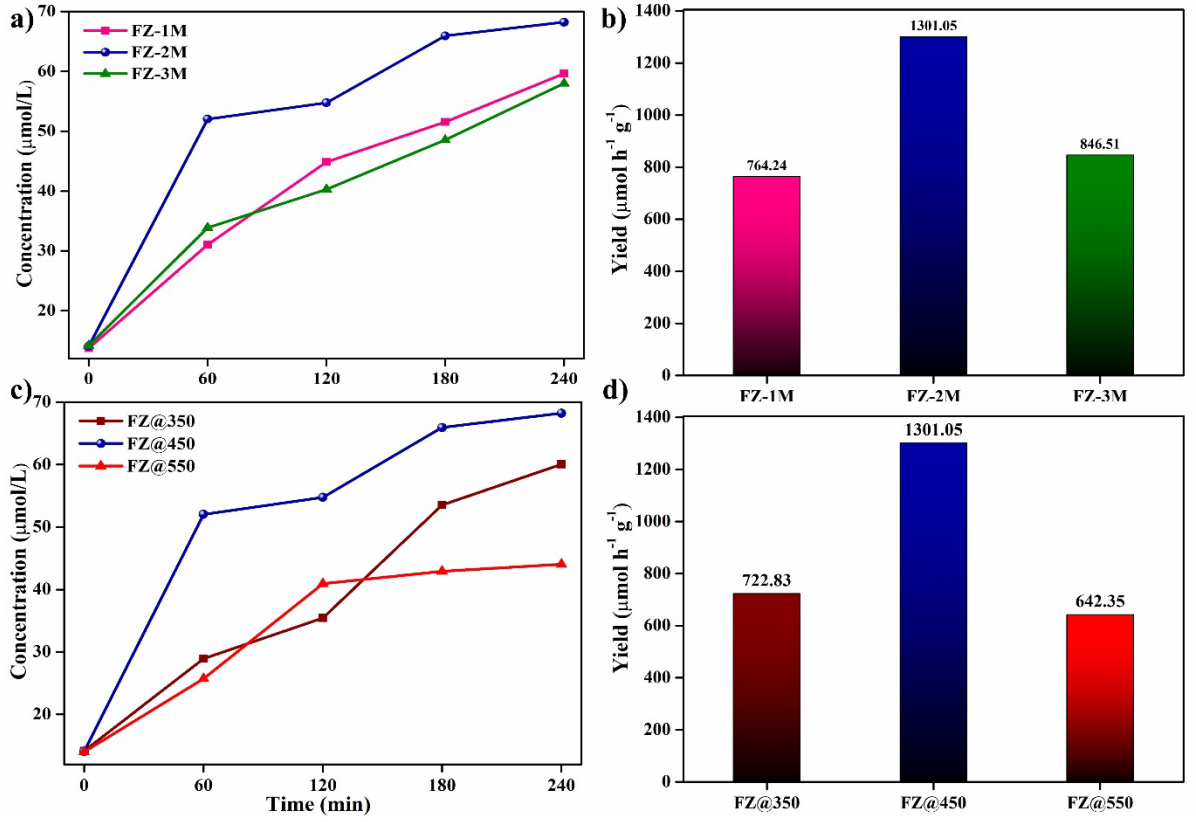

Fig. S16 Comparison of the photocatalytic activity for optimisation studies.

Fig. S17 Experimental setup

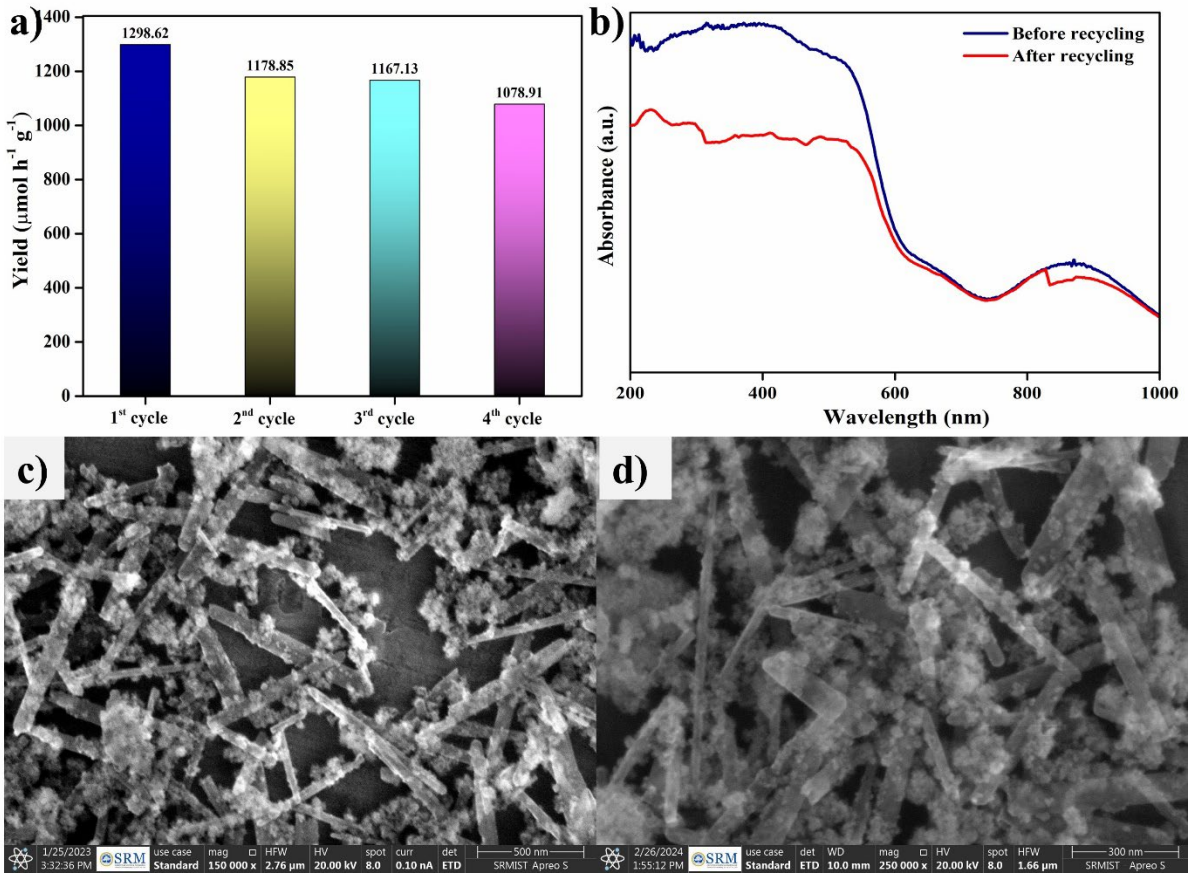

Fig. S18 a) Photocatalytic ammonia production rate in the presence of FZ in the first 3 hours of the cycles, b) UV-DRS spectra of FZ before and after recycling, c,d) SEM images of the FZ before and after recycling, respectively.

Table S1 Atomic weight percentage obtained from EDX spectrum of FZ.

Element	Net Counts	Weight %	Atom %	Formula
O	3945	42.25	77.38	O
Fe	3810	20.01	10.50	Fe
Zr	12682	37.73	12.12	Zr
		100.00	100.00	

Table S2 Calculated conduction band, valence band and bandgap values of the as-synthesised photocatalysts from Mott-Schottky and Tauc plots.

Photocatalyst	Flatband potential (fb)	Conduction Band (CB)	CB (RHE)	Valence Band (VB) (RHE)	Bandgap (E_g) (RHE)
Fe_2O_3	-0.83 V	-0.93 V	-0.32 V	+1.60 V	1.92 eV
ZrO_2	-1.08 V	-1.18 V	-0.57 V	+3.63 V	3.63 eV
FZ	-1.01 V	-1.11 V	-0.50 V	+2.15 V	2.65 eV

Consequently, the conduction bands (CB) and valence bands (VB) of the as-synthesised materials can be evaluated using the Nernst equation (equation 2) and equation 3, respectively.

$$E_{RHE} = E°_{Ag/AgCl} + E_{Ag/AgCl} + (0.059 \text{ X pH}) \text{ --- (2)}$$

$$E_{VB} = E_g + E_{CB} \text{ --- (3)}$$

Where E_{RHE} is the calculated potential vs. RHE, $E_{Ag/AgCl}$ is the measured experimental potential vs. Ag/AgCl electrode, $E°_{Ag/AgCl}$ is 0.197 V, and the pH of the solution is 7 at 25 °C.

Table S3 Comparison of some of the photocatalysts reported for photocatalytic nitrogen reduction reactions.

S. No.	Catalyst	Reaction medium	Light source	Ammonia generation rate	Reference
1.	Ni-incorporated ZrO_2/Bi_2O_3	Water and TEOA	Sunlight	9668.2 μmol h^{-1} g^{-1}	[1]
2.	Fe- doped TiO_2	Water and ethanol	4-W UV lamp, 254 nm.	400 μmol h^{-1} g^{-1}	[2]
3.	BiOCl NSs-Fe 5%	Water	300 W Xe lamp	1022 μmol h^{-1} g^{-1}	[3]
4.	Ov- Bi_2MoO_6	Water and methanol	300 W Xe lamp	1300 μmol h^{-1} g^{-1}	[4]
5.	NiS/g-C_3N_4	Water and methanol	300 W Xe lamp	8.15 mg L^{-1}	[5]
6.	Fe_2O_3/g-C_3N_4	Water and ethanol	300 W Xe lamp	47.9 mg h^{-1} L^{-1}	[6]
7.	g-C_3N_4/ZrO_2	Water and methanol	300 W Xe lamp	1446 μmol h^{-1} L^{-1}	[7]
8.	FeN-CDs/TiO_2@CN	Water and methanol	300 W Xe lamp	9.365 mg h^{-1} g^{-1}	[8]
9.	Cu_2O clusters/MIL-100(Fe)	Water	300 W Xe lamp	51.22 μmol h^{-1} g^{-1}	[9]
10.	Fe_2O_3/ZrO_2	Water	Sunlight	1301.05 μmol h^{-1} g^{-1}	**This work**

References

1 S. C. L. AR, R. Thapa and B. Neppolian, *Catal Today*, 2023, **420**, 114034.

2 G. Song, R. Gao, Z. Zhao, Y. Zhang, H. Tan, H. Li, D. Wang, Z. Sun and M. Feng, *Appl Catal B*, 2022, **301**, 120809.

3 N. Zhang, L. Li, Q. Shao, T. Zhu, X. Huang and X. Xiao, *ACS Appl Energy Mater*, 2019, **2**, 8394–8398.

4 G. Li, W. Yang, S. Gao, Q. Shen, J. Xue, K. Chen and Q. Li, *Chemical Engineering Journal*, 2021, **404**, 127115.

5 X. Hu, L. Wang, W. Zhang, Y. Wang, Z. Liu, X. Wang and X. Yao, *Diam Relat Mater*, 2023, **140**, 110533.

6 S. Liu, S. Wang, Y. Jiang, Z. Zhao, G. Jiang and Z. Sun, *Chemical Engineering Journal*, 2019, **373**, 572–579.

7 H. Mou, J. Wang, D. Yu, D. Zhang, W. Chen, Y. Wang, D. Wang and T. Mu, *ACS Appl Mater Interfaces*, 2019, **11**, 44360–44365.

8 K. Li, C. Sun, Z. Chen, H. Qu, H. Xie and Q. Zhong, *Chemical Engineering Journal*, 2022, **429**, 132440.

9 X. Huang, Y. Shi, C. Liu, Z. Wang, J. Bi, C. Y. Jimmy and L. Wu, *Appl Surf Sci*, 2023, **640**, 158443.